Master thesis and internship[BR]- Master's thesis : Structural modelling, testing and correlation of the Athena X-IFU Aperture Cylinder composite structure and investigation of its thermo-mechanical topology optimisation[BR]- Integration Internship : CSL

Auteur : Puissant, Marie
Promoteur(s) : Bruyneel, Michael
Faculté : Faculté des Sciences appliquées
Diplôme : Master en ingénieur civil en aérospatiale, à finalité spécialisée en "aerospace engineering"
Année académique : 2022-2023
URI/URL : http://hdl.handle.net/2268.2/17436

UNIVERSITY OF LIÈGE
MASTER THESIS

Structural modelling, testing and correlation of the Athena X-IFU Aperture Cylinder composite structure and investigation of its thermo-mechanical topology optimisation

Author:
Marie PUISSANT

Supervisor:
Michael BRUYNEEL

Advisors:
Lionel JACQUES
Jean-Marc VAASSEN

A thesis submitted in fulfillment of the requirements
for the degree of Master Of Science (MSc) in Aerospace Engineering

June 8, 2023

UNIVERSITY OF LIÈGE

Abstract

Faculty of Applied Sciences

Master Of Science (MSc) in Aerospace Engineering

by Marie PUISSANT

X-IFU is one of the two instruments designed to participate in the space mission Athena. Its technology is based on hyper-sensitive captors working at a low temperature close to the absolute zero. To preserve the low temperature near the captors, the structure is designed to minimise the conductivity between the telescope's subsystems.

This thesis aims to study the design of one particular component of X-IFU, the Aperture Cylinder, which provides structural support between two stages of respectively 100K and 300K reference temperatures.

The study starts with the definition of the different requirements imposed by the mission and is followed by a discussion on the choice of the material used to build the aperture cylinder which highlights the interest of GFRP. Samples of a GFRP designed for cryogenic conditions are analysed theoretically based on the theory of composite.

The theoretical study of the material is followed by experimental tests performed on the GFRP samples. First, tests in traction are performed and a corresponding numerical model of the samples is made. Then samples of GFRP, whose shapes are based on the current design of the aperture cylinder, are tested in flexion and bending both numerically and experimentally to assess the behaviour of the composite structure.
Finally, a simplified version of the aperture cylinder is presented and discussed from the boundary conditions, the connections modelling and the modal analysis to a simulation of a random vibration test.

During this thesis, a vibration test on a shaker is performed. The configuration, vibration results and data treatments are presented and discussed to evaluate the different resonance frequencies and the behaviour of the structure.
A correlation between the numerical model and the experimental results is done based on the theoretical results of the composite theory.

Finally, a discussion is made about the interest of topology optimisation to design composite structures and more particularly, to discuss the validity of different optimisation problems. The tool used to performs the optimisation is *OOFELIE* and *TOPOL*.

Acknowledgements

I would like to express my deepest gratitude to my promotor, Michaël Bruyneel as well as my supervisor, Lionel Jacques for their constant advice, encouragement and availability. I would also like to thank Jean-Marc Vaassen for his assistance with the optimisation tools and extend my thanks to André Bertin whom has offered invaluable advice and expertise.

A special thanks to the CSL's engineers and technicians for their help in various technical aspects of this thesis but also for their welcome in the company.

A heartfelt gratitude to my family and friend for their moral support over the last five years. I would also like to express my deepest gratitude to Alexis Bertrand. I could not have undertaken this journey without him. His unwavering support, presence and belief in my work was a great source of motivation and inspiration.

Contents

List of Figures

List of Tables

List of Abbreviations

ATHENA	**A**dvanced **T**elescope (for) **H**igh-**En**ergy **A**strophysics
ApC	**Ap**erture **C**ylinder
CTE	**C**oefficient (of) **T**hermal **E**xpansion
CVCM	**C**ollected **V**olatile **C**ondensable **M**aterial
CFRP	**C**arbon **F**iber **R**einforced **P**olymer
ESA	**E**uropean **S**pace **A**gency
FRF	**F**requency **R**esponse **F**unction
FOSU	**F**actor **O**f **S**afety (of) **U**ltimate design
GFRP	**G**lass **F**iber **R**einforced **P**olymer
MAC	**M**odal **A**ssurance **C**riterion
MMA	**M**ethod (of) **M**oving **A**symptotes
MoS	**M**argin **O**f **S**afety
PPM	**P**eak **P**icking **M**ethod **PSD**
Power **S**pectral **D**ensity	
TES	**T**ransition **E**dge **S**ensors
TML	**T**otal **M**ass **L**oss
WFI	**W**ide **F**ield **I**mager
X-IFU	**X**-ray **I**ntegral **F**ield **U**nit

List of Symbols

A_{ij} (i,j = 1,2,6)	extensional rigidities
B_{ij} (i,j = 1,2,6)	coupling matrix
C	mechanical compliance
C_{ij} (i,j = 1,2,6)	elements of stiffness matrix
C_{th}	thermal compliance
D_x, D_y	flexural rigidities
D_{xy}	twisting rigidity
D_{ij} (i,j = 1,2,6)	flexural rigidities
E	Young's modulus of isotropic material
E_1	Young's modulus of lamina parallel to filament or warp di
E_2	Young's modulus of lamina transverse to filament or warp
E_x	Young's modulus of laminate along x reference axis
E_y	Young's modulus of laminate along y reference axis
f_r	resonance frequency
shear modulus of lamina in 12 plane	GPa
G_{xy}	shear modulus of laminate in xy reference plane
P	power
Q	quality factor
shear force parallel to z axis of sections	of a plate perpendicular to x and y axes, respectively
Q_{ij} (i,j = 1,2,6)	reduced stiffness matrix
V_f	filament content or fiber volume
X_T, Y_T, Z_T	the tensile material normal failure stress
X_C, Y_C, Z_C	the compressive material normal failure stress
$X_{\epsilon T}, Y_{\epsilon T}, Z_{\epsilon T}$	the tensile material normal failure strains
$X_{\epsilon C}, Y_{\epsilon C}, Z_{\epsilon C}$	the compressive material normal failure strains
α	thermal expansion coefficient
$\hat{\alpha}$	amplitude of the resonance frequency
ζ	damping ratio

Chapter 1

Introduction

During ESA Science Programme Committee in 2014, ATHENA, Advanced Telescope for High-Energy Astrophysics, was selected as a class L mission, satisfying the theme "Hot and Energetic Universe". Initially due for launch in 2028, Athena's mission includes two interchangeable focal plane instruments namely the Wide Field Imager (WFI) and the X-ray Integral Field Unit (X-IFU). The mission aims to provide a major leap forward in high-energy observational capabilities by delivering performances greatly exceeding the current X-ray observatories such as XMM Newton and Chandra. The X-IFU instrument technology is based on a large array of Transition Edge Sensors (TES) cooled under 100 mK thereby requiring a cooling system. To ensure the low thermal conditions required by the X-IFU detectors, a Dewar is installed and contains the instrument. The cooling system induces a large thermal gradient through the different subsystems of the cryostat.

Figure 1.1 presents the spacecraft architecture. On the right, the focal plane module supporting both instruments can be seen.

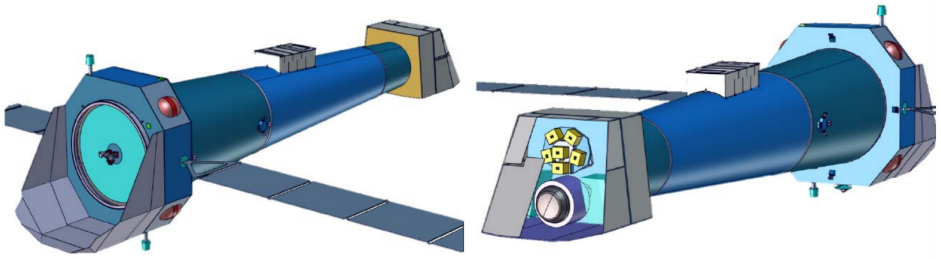

FIGURE 1.1: Athena S/C with Service Module including the mirror assembly (left) and Focal Plane Module integrating the WFI and X-IFU (right).

The aperture cylinder provides mechanical support for three ultra thin aluminium filters blocking the thermal infrared, visible, ultraviolet, and radio-frequency radiations allowing high transmission of X-rays. The filters are 30nm thick with a 45nm support of polyimide and mechanically reinforced by a hexagonal stainless-steel support. Each filter is anchored on different thermal shields of the Dewar. The three filters supported by the aperture cylinder are linked to the outer vessel, the outer cryo-shield or the inner cryo shield and their respective reference temperatures are of 300K, 100K and 30K. Figure 1.2 presents the overall configuration of the aperture cylinder. The present thesis aims at studying the GFRP blades supporting the structure.

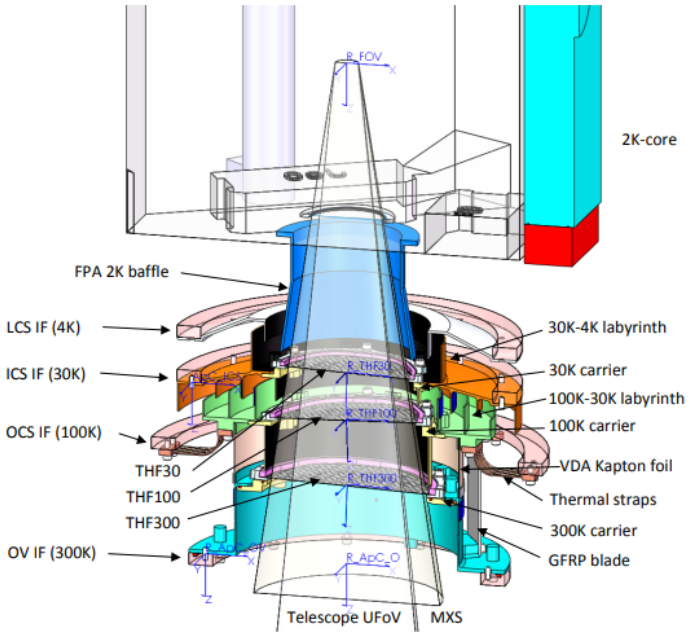

FIGURE 1.2: ApC overall description.

The aperture cylinder containing the optical blocking filter is thus subjected to conflicting requirements. The minimisation of the heat transmitted from the 300K flange to the 100K flange which tends to suppress any material between the two flange. The Apc must also ensure the mechanical support of the filters and upper flange and thus, to prevent the filters' damage. This requirement, on the opposite, tends to maximise the mechanical support provided by the GFRP structure and thus to increase the volume of material. Moreover, the contamination induced by the structure must be minimised to ensure the filter's transparency to X-ray.

Based on these constraints, the CSL conducted a first material selection. It highlighted the interest in composite and more specifically GFRP as a candidate material to construct the support (See purple struts in Figure 1.3). Figure 1.3 shows the current design of the aperture cylinder, which contains twelve struts, in purple on the scheme, linking the 300K and 100K flanges. Theses struts are the focus of the present thesis.

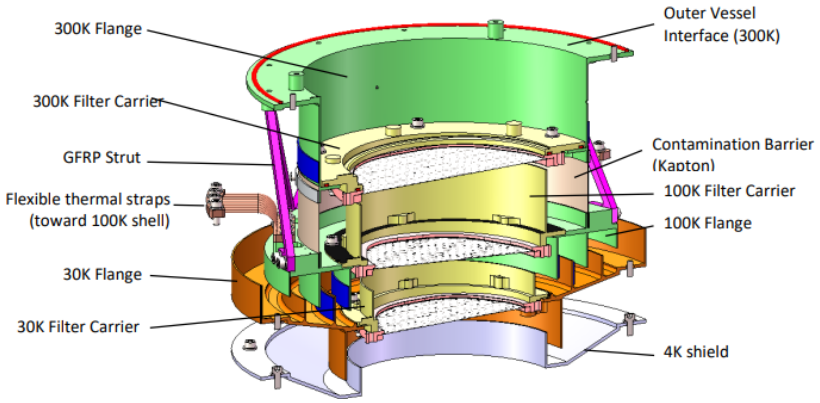

FIGURE 1.3: X-IFUs Aperture cylinder current CAD model.

At the end of 2022, the Athena mission design had to be reevaluated for cost reduction and thus, the design constraint of the aperture cylinder is not precisely defined at the time of this thesis. Since the mission design was remade, the model shown in Figure 1.3 is subjected to changes. Thus the final shape of the connection cannot be established.
The study presented in the following pages aims at evaluating the possibility of GFRP as a material to build the aperture cylinder in a similar environment as presented in Figure 1.3.

The thesis starts by conducting a preliminary material selection to justify the use of GFRP. The material properties are then extensively studied at different scales. The laminate properties are deduced from a ply properties discussion. Different failure theories are presented and a parameter influence study is driven.
Then, traction tests are conducted and reproduced numerically. Deduction on the laminate stacking sequence and ply properties are made from the traction test.
The current shape of the GFRP structure is then analysed to spot its weaknesses and evaluate its performance under different loads. Experimental and numerical tests are done to evaluate the deformation of the structure and the accuracy of the assumptions made on the laminate.
A vibration test on a shaker is finally performed and the eigenfrequencies and behaviour of the structure are evaluated. A numerical model is created and its design is extensively studied. Finally, a dynamic response similar to the vibration tests is done on the numerical model to finalise the correlation between experimental and numerical analysis.
After the current design has been studied, a discussion about the geometry improvement is made based on the observation made through the previous studies.

On a second basis, the aperture cylinder shape is optimised by two topology optimisation tools: *OOFELIE* and *TOPOL*. Multiple optimisation problems are proposed and their solutions are discussed. This topology optimisation starts a discussion about a potential multiphysics optimisation.

Chapter 2

Material Study

2.1 Sub-system requirements

The choice of material used to build the aperture cylinder is made based on a preliminary material selection. This process aims at comparing the general properties of different materials and determining which ones are suitable for the current application without taking into account the precise geometry of the structure. Throughout this material study, three main aspects are compared: the thermal conductivity of each material, their mechanical properties and their outgassing properties. The chosen material is then studied more extensively to validate the choice.

Contamination

ESA provides criteria on the CVCM (Collected Volatile Condensable Material) and TML (Total Mass Loss) for any space application to limit the contamination inside the structure. The filters surrounded by the aperture cylinder must remain clean and the surrounding material must limit the amount of outgassing material. The criteria on the CVCM (<0.1) and TML (<1%) can be found on the *ECSS-Q-ST-70-02C - Thermal vacuum outgassing test for the screening of space materials* [13].

Heat transfer

To restrict the heat transmission from the high-temperature flange (300K) to the low-temperature stage (100K), the heat flow between the two is limited to a value Q_{max} of 0.5W. While the geometry is critical to obtain such a low thermal transmission, it still indicates that the coefficient of thermal conductivity must be minimised.

Mechanical support

The young modulus of the material is also a critical criterion but its limiting value is unknown. The global subsystem, however, must have a first eigenfrequency above 150Hz. This value ensures that the resonance frequency of the aperture cylinder does not amplify other sub-systems' own resonance frequencies. In this chapter, the first frequency is not directly computed. However, the structure is expected to sustain a 25G acceleration during the vibration tests. Since the resonance frequencies are directly proportional to the material Young Modulus, a high value of the latter is desired.

2.2 Material properties comparison

From the different requirements defined in section 2.1, two parameters are retained: the conductivity and the young modulus. The first frequency of the aperture cylinder is calculated further in the report as a consequence of the selected material and geometry but is not used in the preliminary study.

2.2.1 ApC geometries

The comparison between the materials is based on simplified geometries of the cylinder:

- A hollow cylinder
- A set of three bars linking the first stage and second stage of the aperture cylinder

These geometries are used to evaluate the heat flux between the two stages.

As the inner diameter of the cylinder must let the light pass through the filters of X-IFU, its inner value is based on the geometry of the aperture cylinder showed in Figure 1.3 and is thus set to 200mm and the height of the cylinder to 100mm, still based on the geometry shown in Figure 1.3.
The bars geometry proposed is: 100x36x3mm^3 (h x L x t).

2.2.2 Parameters of comparison

The comparison of the materials focuses on two main parameters: the young modulus to conductivity ratio to be maximised and the maximum amount of material allowed to limit the amount of heat transferred Q_{max} to 0.5W. The latter parameter assumes first the aperture cylinder shaped has a ring and then, with a more reasonable geometry, considers the connections as bars linking the two stages. For the full cylinder geometry, the quantitative parameter is the thickness of the cylinder allowed. For the bars' geometry, it simplifies to a round number of bars allowed before violating the heat transfer criterion.

To guarantee the possibility to use a reasonable quantity of material without violating the maximal heat transferred between the two stages, the conductivity equations are applied in the case of a hollow cylinder and the case of multiple bars. The maximal heat transfer coefficient can be derived from the maximal heat flux required:

$$G_L = \frac{Q_{max}}{\delta T} = \frac{0.5}{300 - 100} = 0.0025\text{W/K}, \tag{2.1}$$

And from the maximal heat transfer coefficient, the maximal thickness of the cylinder and the maximal number of bars can be found.

Cylinder maximal thickness

Since the cylinder height is set, the maximal section of the cylinder is evaluated. Knowing the inner diameter, the maximal thickness can be deduced.

$$S_{max} = \frac{G_L h}{k} \tag{2.2}$$

$$t_{max} = \sqrt{\frac{S_{max}}{\pi} + r_i^2} - r_i. \tag{2.3}$$

where $r_i = 0.2$mand h = 0.1m.

Maximal number of bars

The section and height being known, the number of bars can be directly deduced from the heat flux coefficient:

$$N_{bars,max} = \frac{G_L.h}{S}. \tag{2.4}$$

where S=0.036x0.003m² and h = 0.1m

2.2.3 List of materials

The materials usually used for space applications are listed in the table below with their conductivity at different temperatures and their Young Modulus. The ratios between the two properties are also listed. In addition to the common value of the different materials, a fabric GFRP made for cryogenic conditions called *VETRONIT Cryo* is added. This material is made especially for low conduction desired structures.

		Al 6061T6	AISI 304	Ti6Al4V	Kel-F	Vespel	G10	Al 6N	CFRP Epoxy	HMCF	GFRP VETRONIT Cryo
CONDUCTIVITY	300	160	15	7	0,27	0,35	0,7	237	6,82	155,60	0,3
k $[\frac{W}{mK}]$	200	136		5,7	0,27		0,6	237			
	100	98		3,8	0,24		0,4	302			
YOUNG	300	69	193	112	1,4	3,3	25	400	44.9	85	22
MODULUS	200	74		116	3,4		27				
E [GPa]	100	77		120	6,2		30				
E/k$[\frac{GPamK}{W}]$		0,43	12,87	16	5,19	9,43	35,71	0,08	6,58	0,55	73,33

TABLE 2.1: Properties of different materials suitable for space applications.

High-pressure fibreglass laminates (G10) offer the highest ratio followed by titanium whose ratio is less than half of the laminate one. G10 materials refer to any form of composite material with continuous filament fiberglass cloth with epoxy resin system. The G10 class is described by the norm NEMA LI 1-1998 Grade G-10. This first intuitive comparison, however, does not ensure a sufficiently low thermal coefficient.

The equations described from Equation 2.3 to 2.4 are applied to the different materials' properties:

	Al 6061T6	AISI 304	Ti6Al4V	Kel-F	Vespel	G10	Al 6N	CFRP Epoxy	HMCF	GFRP VETRONIT Cryo
Thickness t [µm]	2	27	57	1463	1130	567	2	58	3	1318
N bars	0	0	0	8	6	3	0	0	0	7

TABLE 2.2: Maximal allowable cylinder thickness and number of bars.

Only the Kel-F, Vespel and G10 allow such a configuration. The maximal thickness allowed of 1.4mm is made of Kel-F since its conductivity is the lowest. With a cylinder made of high-pressure fibreglass laminate, the thickness drops to 0.56mm and with the GFRP made especially for low temperatures, the thickness maximal value is 1.3mm.
More intuitively, the number of bars allowed to build a structure is above three for four of the selected materials. The Kel-F has the highest value with 8 bars at maximum. Regular G10 only provides three bars but the VETRONIT version extends this value to 7.
By having the highest Young modulus, high-pressure fibreglass laminate appears as a potential solution. The other solutions proposed might not sustain the structure design loads since they have low modulus compared to G10. Moreover, the GFRP made for low temperature decreases greatly the value of the conductivity compared to a regular G10. The VETRONIT Cryo fabric is thus considered a potential material for the support between the two stages.

2.3 GFRP Laminate analysis

The material study conducted in section 2.2 highlighted the potential of GFRP to build the aperture cylinder and is now studied in more detail. The following pages aim at assessing the behaviour of the material and the influence of different parameters describing the composite selected in section 2.2 called VETRONIT Cryo GFRP fabric. Since the material properties given by the manufacturer are not complete, the first objective of this section is to evaluate the properties of one ply. From there, the properties are modified to obtain the global material properties to complete the missing information. These properties must be defined to create a design and, further in the study, evaluate the behaviour of the whole structure. The maximum stress, maximum strain, Tsaï-Wu and Tsaï-Hill failure criteria are also defined and applied for defined load cases on an infinite plate. The online tool *Coexlam* by *Coexpair* is used to evaluate the design failure criteria. The most critical criterion is established and serves as a basis for a parameter influence study. In addition, a deformation test is made on samples made of VETRONIT Cryo GFRP fabric for different load cases.

This study eases the correlation method based on tensile and compressive tests made on struts samples whose properties are not fully known (See chapter 3). In the same manner, the influence of the parameters is also of use in the correlation made on the shaker tests made in chapter 5. The samples' pictures are displayed in Figure 2.1.

FIGURE 2.1: 0°orientation sample used for traction-compression tests.

The known properties of the composite are given in Table 2.3

Property	**Unit**	**Value**	**Test norm**
Modulus of elasticity	MPa	22000	ISO 178
Shear strength	MPa	30	ISO 178
Compressive strength	MPa	300	ISO 604
Tensile strength	MPa	300	ISO 527
Density	g/cm^3	1.83	ISO 1183
Coefficient of linear expansion	$10^{-6}/K$	15	DIN 53752
Thermal conductivity	$W/(m.K)$	0.3	DIN 52612
Collected volatile condensable material	%	0.01	ASTM E 595
Total mass loss	%	0.15	ASTM E 595
Minimal thickness of sample	mm	0.2	-

TABLE 2.3: VETRONIT Cryo GFRP properties by VonRoll.

The ply thickness is required to analyse the ply and laminate properties. However, Table 2.3 only refers to the minimal sample available for order. The ply thickness can be evaluated with an inspection of the width of the samples used for the traction tests. The Figure 2.2 presents a close-up view of a sample cross-section. The total number of plies is 29 and the measured thickness is around 5.5mm. Dividing the thickness by the number of plies gives a ply thickness of around 0.19mm. For simplicity and to fit the actual minimal value of the sample, the thickness value is approximated as 0.2mm.

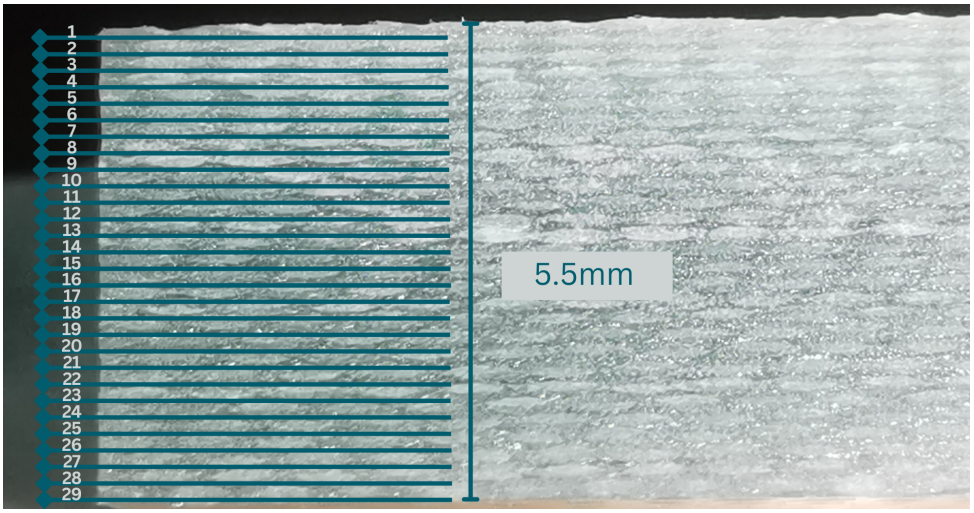

FIGURE 2.2: Zoom on 0°orientation traction-compression sample plies.

2.3.1 Ply properties

The composite defined in Table 2.3 is composed of fabric plies whose properties are unknown. A single ply is made with 2 orientations of fibres perpendicular one to another. This combination can be seen on Figure 2.1 as the surface appears as a woven fabric. These angles are defined as 0° and 90°. The properties of such a fabric can be retrieved from two superposed unidirectional plies. Their values can be found in the CMH-17 composite reference book *Composite Material Handbook* [7] and are displayed in the Table 2.4.

Property	Unit	Value
E_1	MPa	45000
E_2	MPa	12500
ν_{12}	-	0.27
G_{12}	MPa	4500
ρ	g/cm^3	1.85
V_f	%	52
t	mm	0.2

TABLE 2.4: Glass Fiber unidirectional tape from *Composite Material Handbook* [7].

The properties of two unidirectional tapes superposed at 0° and 90° can be computed using the lamination theory.

General constitutive equations

First, a thin anisotropic plate is assumed. Neglecting the thermomechanical terms, its constitutive equation can be written as:

$$\begin{bmatrix} N \\ M \end{bmatrix} = \begin{bmatrix} A & B \\ B & D \end{bmatrix} \begin{bmatrix} \epsilon \\ \kappa \end{bmatrix} \tag{2.5}$$

where A_{ij}, the membrane stiffness matrix, B_{ij} the coupling matrix and D_{ij} the flexural and bending stiffness matrix can be defined as:

$$A_{ij} = \sum_{k=1}^{n} \left(Q_{ij}\right)_k \left(h_k - h_{k-1}\right), \tag{2.6}$$

$$B_{ij} = \sum_{k=1}^{n} \left(Q_{ij}\right)_k \left(h_k^2 - h_{k-1}^2\right)/2, \tag{2.7}$$

$$D_{ij} = \sum_{k=1}^{n} \left(Q_{ij}\right)_k \left(h_k^3 - h_{k-1}^3\right)/3. \tag{2.8}$$

where h_k refers to the ply k bottom location.

The reduced stiffness matrix has to be defined for both plies: one at 0° and one at 90° from the rotation of the stiffness matrix in the material axis. The reduced stiffness matrix in the material (orthotropy) axis can be written as:

$$Q_{x,y,z} = \begin{bmatrix} Q_{xx} & Q_{xy} & 0 \\ Q_{yx} & Q_{yy} & 0 \\ 0 & 0 & Q_{ss} \end{bmatrix} = \begin{bmatrix} mE_x & m\nu_{yx}E_x & 0 \\ m\nu_y E_y & mE_y & 0 \\ 0 & 0 & G_{xy} \end{bmatrix}, \tag{2.9}$$

$$\nu_{yx} = \frac{\nu_{xy}E_y}{E_x}, \tag{2.10}$$

$$m = \frac{1}{1 - \nu_{xy}\nu_{yx}}. \tag{2.11}$$

Each element of the matrix $Q_{x,y,z}$ can thus be retrieved from the 4 independent elastic constants E_x, E_y, G_{xy} and ν_{xy} whose values are presented in Table 2.4.
Once the stiffness matrix in the material axis $Q_{x,y,z}$ is computed, the matrix is rotated according to the structural axis to obtain the matrix $Q_{1,2,3}$. The 0° and 90° plies of UD glass fibre have different matrices $Q_{1,2,6}$.
A rotational matrix can be used to proceed to the rotation but its effect on the 0° and 90° plies are known. For the 0° ply, the structural coordinates does not modify the values found in Equation 2.9 and thus $Q_{1,2,3}$ is equal to $Q_{x,y,z}$. For the ply rotated by 90°, the values of Q_{11} and Q_{22} are simply exchanged. From there, the matrices A_{ij}, B_{ij} and D_{ij} can be computed using Equation 2.6 to 2.8.

Average ply elastic constants

The average ply elastic constants can be obtained from the matrix of laminate stiffness A defined in Equation 2.6.

$$E_{xx} = \frac{A_{11}A_{22} - A_{12}^2}{A_{22}t} \sim 29000\text{MPa}, \tag{2.12}$$

$$E_{yy} = \frac{A_{11}A_{22} - A_{12}^2}{A_{11}t} \sim 29000\text{MPa}, \tag{2.13}$$

$$G_{xy} = \frac{A_{66}}{t} \sim 4500\text{MPa}, \tag{2.14}$$

$$\nu_{xy} = \frac{A_{12}}{A_{22}} \sim 0.12, \tag{2.15}$$

$$\nu_{yx} = \frac{A_{12}}{A_{11}} \sim 0,12. \tag{2.16}$$

2.3.2 Laminate properties

The laminate properties are evaluated from the single-ply elastic constants computed in section 2.3.1.
The same procedure as depicted in subsection 2.3.1 is done for the average laminate properties. However, the elastic properties in the material axis used are replaced by the average ply properties previously computed. The stacking sequence is not known and must be discussed

Stacking sequence

The stacking sequence of the Vetronit Cryo laminate is not clearly defined but can be estimated from the information such as the minimal ply thickness and the samples received from the manufacturer. The number of plies is not known either. The current industry ply thickness can go down to 0.2mm which is also the minimal sample thickness available by the manufacturer and the sample of GFRP in a Z-shape is 5mm thick. This assumption gives a total of 25 plies of 0.2mm each.

The Young Modulus presented in Table 2.3 does not indicate any preferential direction therefore, two possibilities are considered. The first one is a quasi-isotropic stacking sequence and the second is that all plies have the same orientation. First, the single orientation hypothesis is analysed.

Single orientation Laminate This first stacking sequence assumed simply to stack the 25 plies in the same direction. The properties of such a laminate do not present particular relations between the different matrices as it is described in the next paragraph. As the plies are simply glued one above the other in the same direction, the Young modulus and shear modulus of the laminate are the same as the ones of a single ply. The laminate is easy to manufacture but decreases greatly the properties in directions other than the direction of the fibres at 0 and 90°.

Quasi-isotropic laminate The stacking sequence in this section must be balanced, symmetric and quasi-isotropic. Thus the number of plies at each angle (0°, 45°, 90° and $-45°$) must be equal. The number of plies being odd, a central ply will define the symmetry. The design rules stated lead to the selection of the following stacking sequence:

$$[(0/+45/90/\text{-}45)_3/\overline{0}]_s$$

As the composite is made of fabric with two perpendicular orientations, the 0° and 90° as well as $-45°$ and $+45°$ are similar. Following the laminate orientation code is based largely on the code used in the *DOD/NASA Advanced Composites Design Guide* [10], the stacking sequence can be reduced to:

$$[(0/45)_6/\overline{0}]_s$$

where the subscript *6* denotes the repetition of the sequence, *s* the symmetry of the stacking sequence and $\overline{0}$ indicates that the symmetry starts from the centre of the ply.

When designing a quasi-isotropic laminate, the in-plane properties follow the rules presented in Equation 2.17.

$$A_{11} = A_{22}, \qquad A_{16} = A_{26} = 0, \qquad \text{and } A_{66} = \frac{A_{11} - A_{12}}{2}. \tag{2.17}$$

This relation can be verified by applying the lamination theory described in the previous pages. The result is indicated in the following equation:

$$A_{11} = A_{22} = 126847\text{MPa}, \qquad A_{26} = -A_{16} = 0.027\text{MPa}$$

$$\text{and } A_{66} = 42771 textMPa \approx \frac{A_{11} - A_{12}}{2} = 44460\text{MPa}. \tag{2.18}$$

The two first relations are respected with a small residue for the second relation. The third one has a deviation of 4%. Another stacking sequence can be tested to reduce this error or later on to be tested for numerical simulation such as:

$$[(0/15/30/45/60/75)_2/\bar{0}]_s$$

which uses less conventional angles. Increasing or decreasing the thickness can be considered during the correlation.

Average laminate properties

Quasi-isotropic laminate Assuming the stacking sequence is quasi-isotropic, the average laminate elastic properties can be evaluated using the results found in Equation 2.18 and replacing them in the equations 2.12 to 2.16. The results obtained are:

$$E_{xx} \sim 23100\text{MPa}, \tag{2.19}$$
$$E_{yy} \sim 23100\text{MPa}, \tag{2.20}$$
$$G_{xy} \sim 8555\text{MPa}, \tag{2.21}$$
$$\nu_{xy} \sim 0.3, \tag{2.22}$$
$$\nu_{yx} \sim 0.3. \tag{2.23}$$

The Young Modulus found is close to the 220GPa given in the data sheet 2.3. Since the Young modulus and shear modulus selected do not represent the exact values of the GFRP fabric used for the tests but an estimation based on common GFRP properties, their amplitude can be decreased during the correlation process without leaving the range of existing values for this material.

Even though this result is a good first approximation, other solutions of stacking sequence can be considered. Intensive study is not required but some tendencies can be spotted.

Increasing the thickness of each ply to 0.25mm and thus lowering the number of plies down to 20, induces less than 3% of variation for each property: -1.2% for the Young modules, +2% for the shear modulus and 3% for the Poisson ratio.
Decreasing the thickness to 0.1mm however, does not induce any modification neither in the average properties of the laminate or the in-plane matrix A but modifies

the out-of-plane matrix D such that it gets closer to a homogeneous laminate whose relation is similar to the one presented for quasi-isotropic laminate:

$$D_{11} = D_{22}, \qquad D_{16} = D_{26} = 0, \qquad \text{and } D_{66} = \frac{D_{11} - D_{12}}{2}.$$

$$A_{ij} = \frac{12}{h^2} D_{ij}. \tag{2.24}$$

In conclusion, increasing the number of plies for a quasi-isotropic stacking sequence upgrades the isotropic behaviour. In reality, the plies thickness cannot be decreased down to 0.1 as the minimal plies thickness is 0.2, so an increase of the laminate global thickness would be required. However, increasing the section also increases the conduction in the structure.

One-direction laminate When the fibres are all oriented in the same direction the global laminate properties are similar to the properties of the single ply. The laminates properties are then:

$$E_{xx} \sim 29000\text{MPa}, \tag{2.25}$$
$$E_{yy} \sim 29000\text{MPa}, \tag{2.26}$$
$$G_{xy} \sim 45000\text{MPa}, \tag{2.27}$$
$$\nu_{xy} \sim 0.12, \tag{2.28}$$
$$\nu_{yx} \sim 0.12. \tag{2.29}$$

2.3.3 Design failure criteria

The suitability of a material for any application is first validated by its ability to sustain critical load cases. These load cases are defined from the structure solicitations expected during its life majored by a safety factor. In composite material, defining if the design criteria are met by the design is more complex than with conventional material such as metal as the failure criteria are themselves more complex. This section briefly introduces the most common failure criteria with their specificity, applies them to different load cases and spot the most critical one.

Before studying complex geometry behaviour under different load cases, the laminate can be investigated on a core level. The current shape of the aperture cylinder composite structure is computed numerically further in the report.

Common failure criteria

The usual failure criteria used in composite failure theory are the maximum stress, maximum strain, Tsaï-Wu and Tsaï-hill criteria applied to unidirectional fibre composite laminate and laminate as stated in Jacob Aboudi [19]. The failure theories applied to specific fabrics laminate are validated by the study conducted in Daniel, Luo, and Schubel [8].

Failure in composite material being more complex than failure occurring in an isotropic material, a brief definition is given by Daniel, Luo, and Schubel [19]: *"The point at which the applied loading can no longer be safely supported may be thought of as "failure". It may correspond to an actual failure, fracture, or other loss of structural integrity of a specimen in an experiment, but in design, failure more generally refers to exceeding some limit or criterion that has been established to assess the ability to support loads safely."*.

This failure can occur at different scales inside the laminate. At the constituent level, the different failures are matrix cracking, fibre breakage, debonding between the fibre and the matrix, and microbuckling of the fibre. Other failure types can be defined from the laminate level. These are the complete laminate fracture, delamination between the plies but also the ply cracking or splitting as well as fibre bridging.

A given point in a structure is safe if the allowables are not exceeded by the stress and strains supported by the structure. These allowables are thus critical in the use of failure theory. Their values can be found in Table 2.3 as the shear, compressive and tensile strengths. With a balanced material, the allowables in the transverse and warp directions are equal.

The margin of safety can be defined as the part of the load that can be added to reach failure in the plies. Mathematically, the margin of safety is written differently depending on the method used to compute the failure.

Maximum stress theory Simply compares the stress to the allowables but no interaction between the stresses is considered. Failure is considered when the following restrictions are not respected:

$$X_C < \sigma_{11} < X_T \qquad Y_C < \sigma_{11} < Y_T \qquad |\tau_{12}| < S$$

The margin of safety is calculated as the additional load which can be applied to reach the exact load at which failure is guaranteed.

$$MoS = \frac{\text{allowable stress}}{\text{applied stress}} - 1; \tag{2.30}$$

Maximum strain theory Identical to the maximum stress criterion with the limit expressed in strain:

$$X_{\epsilon C} < \epsilon_{11} < X_{\epsilon T} \qquad Y_{\epsilon C} < \epsilon_{11} < Y_{\epsilon T} \qquad |\tau_{12}| < S_\epsilon$$

The margin of safety is calculated as the additional load which can be applied to reach the exact load at which cracks inside the laminate will propagate.

$$MoS = \frac{\text{allowable strain}}{\text{applied stress}} - 1; \tag{2.31}$$

Tsaï-Hill Interaction between stresses is considered and failure occurs when the Tsaï-Hill given in Equation 2.32 is greater than one. The values of the allowables switch between compressive and tensile strength depending on the stress values. This property may induce major modifications in the TH function.

$$TH = \frac{\sigma_{11}^2}{X^2} + \frac{\sigma_{22}^2}{Y^2} + \frac{\sigma_{33}^2}{Z^2} + \frac{\tau_{23}^2}{Q^2} + \frac{\tau_{13}^2}{R^2} + \frac{\tau_{12}^2}{S^2} - \sigma_{11}\sigma_{22}\left(\frac{1}{X^2} + \frac{1}{Y^2} + \frac{1}{Z^2}\right) - \sigma_{11}\sigma_{33}\left(\frac{1}{X^2} + \frac{1}{Y^2} + \frac{1}{Z^2}\right) - \sigma_{22}\sigma_{33}\left(\frac{1}{X^2} + \frac{1}{Y^2} + \frac{1}{Z^2}\right) \quad (2.32)$$

$$\text{where} \quad X = X_{T,C}\sigma 11 \qquad Y = Y_{T,C}\sigma 22 \qquad Z = Z_{T,C}\sigma 33 \quad (2.33)$$

Tsaï-Wu Resolves the instantaneous major modification problem in the Tsaï-Hill theory. Interactions between the stresses are also considered. The set of equations relative to the Tsaï-Wu equation is shown on the following quadratic-function inequality:

$$F_1\sigma_1 + F_2\sigma_{22} + F_{11}\sigma_{11}^2 + F_{22}\sigma_{22}^2 + F_{66}\sigma_{12}^2 - \sigma_{11}\sigma_{22}\sqrt{F_{11}F_{22}} < 1, \quad (2.34)$$

$$\text{where} \quad F_1 = \frac{1}{X_t} + \frac{1}{X_c} \qquad F_2 = \frac{1}{Y_t} + \frac{1}{Y_c} \qquad F66 = \frac{1}{S^2}$$

$$\text{and} \quad F_{11} = -\frac{1}{X_t X_c}F_{22} \qquad F_{22} = \frac{1}{Y_t Y_c}$$

Load cases

An infinite plate with 5mm thickness is considered with the load sign convention described on the Figure 2.3.

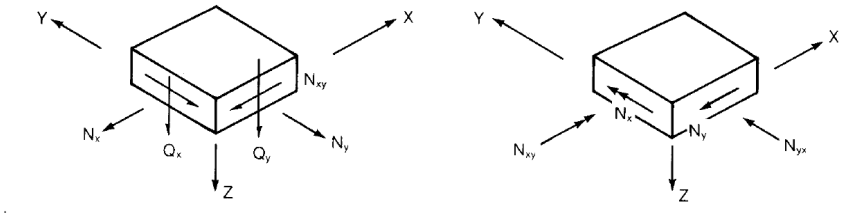

FIGURE 2.3: Laminate Load Sign Convention.

The load cases selected in this study are set to obtain margin values between 0 and 2 to ease the comparison between the different values.

Load / Case	N_x N/mm	N_y N/mm	N_{xy} N/mm	M_{xx} N	M_{yy} N	M_{xy} N
1	400	0	0	0	0	0
2	1000	1000	0	0	0	0
3	0	0	200	0	0	0
4	0	0	0	400	0	0
5	0	0	0	0	0	100

TABLE 2.5: Load cases.

The corresponding margin of safeties for the quasi-isotropic case can be found in the following table:

MoS	Max stress	Max strain	Tsaï-Hill	Tsaï-Wu
1	0,48	0,48	0,45	0,45
2	0,5	0,5	0.70	0.5
3	0,43	0,43	0,43	0,43
4	0,39	0,39	0,36	0,36
5	1,28	1,28	1,28	1,28

TABLE 2.6: Margin of safeties based on different failure theories and load cases for quasi-isotropic laminate.

The maximum stress and strain theories and, apart from the load case number 2 with equal loads in X and Y directions, Tsaï-Hill and Tsaï-Wu have the same values. The load case with only rotation around the N_{xy} direction, called M_{xy}, gives similar results for all safety factors, the same goes for load case 3.
It can be noted that pulling in two directions at the same time increases the margin of safeties as it can be seen when comparing the load cases 1 and 2. For almost the same margin of safety, the load in N_x direction is multiplied by 2.5.

For the case where the plies are in the same directions, the margins are also computed and displayed in Table 2.7.

MoS	Max stress	Max strain	Tsaï-Hill	Tsaï-Wu
1	2.25	2.25	2.25	2.25
2	0,5	0,5	0.70	0.5
3	-0.25	-0.25	-0.25	-0.25
4	2.125	2.125	2.125	2.125
5	0.25	0.25	0.25	0.25

TABLE 2.7: Margin of safeties based on different failure theories and load cases for plies with unique direction.

Without any surprise, the margin greatly increased for loads applied in the fibre direction and decreased for the load applied between 0° and 90°.

Design factor of safety

Now that the comparison between the two staking sequences' margin of safety for different load cases is done, a simple evaluation of the actual design load can be done.

To have an idea of the loads under which the material could be subjected, a quick computation is made based on the acceleration expected during the vibration test on the shaker. The maximal acceleration targeted is 30G.

First, the total mass supported by the aperture cylinder is estimated to be of 1.3kg. During the vibration test, the 100K flange is replaced by a 1.37kg aluminium structure. This mass is thus used in the following computation. As explained above, the current failure criteria evaluations are assuming an infinite plate. Since no width

or length but only the thickness of the laminate is considered, the loads applied are measured in Newtons/millimetre and the moments in Newtons.

The current design presented in Figure 1.3 contains 5mm thick struts. This value is thus kept for the study.

$$F = ma = 1.37 * 30 * 9.81\ 403\ \text{N},$$
$$F_{lin} = \frac{F}{t} = \frac{403}{5} = 80.6\text{N/mm}.$$

The total resulting load is 80.6 N/mm for the twelve struts contained in the current design. This critical value can be now compared to the results obtained using *Coexlam* and ESA's factors of safety.

For reference, ESA set an ultimate design factor of safety (FOSU) of 1.25% for FRP (fibre-reinforced polymer). The FOSU is defined as the multiplying factor applied to the design limit load in order to calculate the design ultimate load (See *ECSS-E-ST-32-10C Rev.1 - Structural factors of safety for spaceflight hardware* [11]). Multiplying the maximal load by 1.25, the ultimate load under 30G is F_{lim} = 100.75N/mm. The quasi-isotropic support this value even in shear since a load of 200N/mm does not lead to failure. For only one direction of ply stacking sequence, a shear load of 100N/mm gives a MoS of 0.5. The material validates the requirement for both cases.

Moreover, this value assumes that one bar supports the whole 1.37kg of the 100K flange. In practice, the load cannot be assumed as equally distributed but a single strut will not support all the loads, so the value of F_{lim} is kept as a critical value which shouldn't be reached. This first approximation suggests that the material is suitable for the loads expected.

Parameter influence study

A parameter influence study is presented in Table 2.9. The failure criterion retained is Tsaï-Wu and the laminate is assumed quasi-isotropic. The different properties of the GFRP are subjected to modifications of ±10% and ±20% with their nominal value. As a reminder, the first estimations of the plies properties are presented in Table 2.8 and the Table 2.5 presents the 5 different loads cases.

Property	Unit	Value
E_{11}	MPa	29000
E_{22}	MPa	29000
ν_{12}	-	0.12
G_{12}	MPa	4500
$X_{t,c}$ & $Y_{t,c}$	MPa	300
S	MPa	30

TABLE 2.8: 0/90 fabric ply properties evaluated.

		CASE 1	CASE 2	CASE 3	CASE 4	CASE 5
difference	E_{11} , E_{22} [MPa]	MoS %				
-20%	23200	-46,67	0,00	-49,17	-56,31	-24,53
-10%	26100	-22,77	0,00	-25,08	-27,34	-10,51
10%	31900	24,31	0,00	-39,17	29,81	10,16
20%	34800	47,53	0,00	47,18	57,96	24,92
	G_{12} [MPa]					
-20%	3600	59,06	0,00	59,22	71,92	31,10
-10%	4050	26,90	0,00	25,77	32,95	13,93
10%	4950	-20,61	0,00	-22,89	-24,72	-11,05
20%	5400	-38,64	0,00	-41,14	-46,63	-20,41
	n_12 [-]					
-20%	0,096	6,02	0,00	4,28	7,62	2,90
-10%	0.108	3,42	0,00	1,61	4,46	1,53
10%	0.132	-1,63	0,00	-3,55	-1,66	-1,12
20%	0.144	-4,07	0,00	-6,05	-4,63	-2,40
	$X_{t,c}$ & $Y_{t,c}$ [MPa]					
-20%	240	-2,49	-60,00	-1,00	-2,86	0,19
-10%	270	-0,55	-30,00	-1,00	-0,41	0,19
10%	330	1,93	30,00	-1,00	2,70	0,19
20%	360	2,74	60,00	-1,00	3,73	0,19
	S [Mpa]					
-20%	24	-61,98	0,00	-67,31	-72,23	-35,47
-10%	27	-30,40	0,00	-34,15	-35,23	-17,64
10%	33	31,78	0,00	32,16	37,53	18,03
20%	36	62,32	0,00	65,32	73,21	35.86

TABLE 2.9: Parameters influence study of Tsaï-Wu MoS under the quasi-isotropic laminate hypothesis.

The allowables are the only parameters influencing the load case with equal loads applied to X and Y axis. For other cases, the shear modulus and strength have the strongest influence on the margin of safety followed by the Young modulus. These tendencies are used to correlate the traction and compression test in chapter 3.

Chapter 3

Traction testing

3.1 Introduction

With the first evaluation of all the material properties done, this section can now cover the second part of the correlation process. Even though some properties are given by the manufacturer, tests are made to reevaluate the principal properties such as the Young modulus and the shear modulus. The tests determine the real critical load value leading to failure and are compared to the numerical simulation reproducing the tensile test configuration and aim at validating the quasi-isotropic or single orientation assumption made on the fabric. This numerical model is studied intensively and gives visible information about the stress concentration and the margin of safety distribution between the plies. It also determines which ply reaches failure first and the impact of the orientation on the results.

3.2 Testing description

3.2.1 Sample preparation for the tests

Figure 3.1 presents the geometry of the samples used for the traction tests and Figure 3.2a, 3.2b and 3.2c show a close picture where the orientation is visible with bare eyes. Three orientations are studied: the warp direction parallel to the sample X axis, with a 45°inclination and finally with a tilt of 7°. This last angle is selected to reproduce the tilt present in the strut built for the current geometry chosen. This geometry with the tilt angle of 7°is presented in chapter 4.

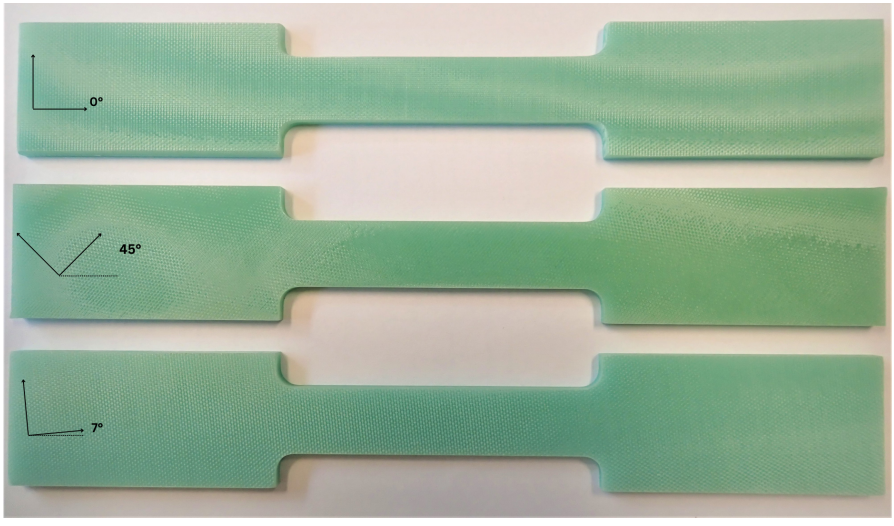

FIGURE 3.1: Samples of GFRP fabric with 0°, 7°and 45°orientation.

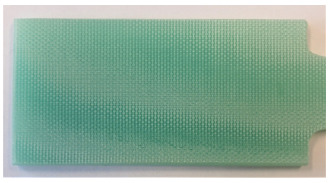

(A) 0°tilt sample.

(B) 7°tilt sample.

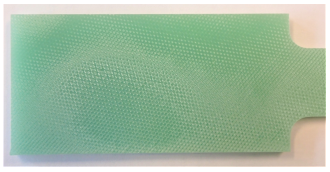

(C) 45°tilt sample.

FIGURE 3.2: Close picture of the three sample orientations.

The samples are 225mm long with a large section of 40mm and a small section of 20mm. The thickness is 5.5mm. In order to proceed to the tests, aluminium plates are glued to the samples' extremities. It was noted that some plates were not straight in the plane nor aligned with the edges of the sample. A sample ready to start the test is presented in Figure 3.3.

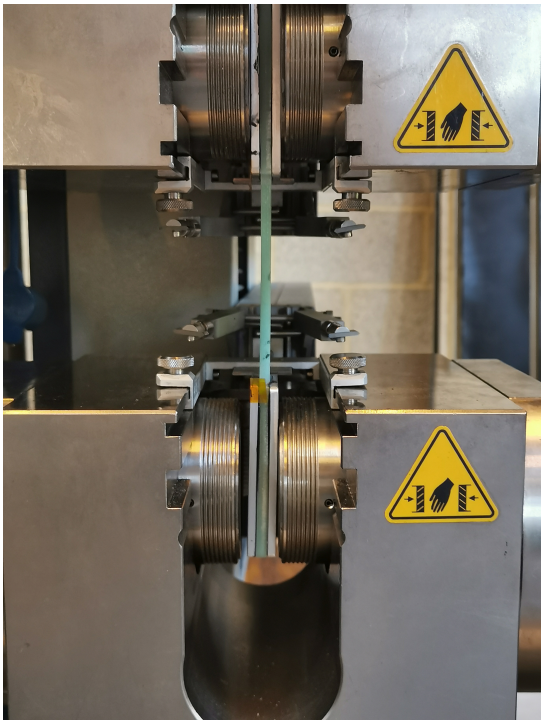

FIGURE 3.3: Clamped sample before the test.

3.2.2 Results

The tensile strength is the load applied to the structure leading to failure divided by the original cross-section of the material. The samples have a cross-section of around 5.5x20mm but each sample cross-section is measured individually by a palmer. As the measurements done are the displacement of the sample in the traction direction and the force required to obtain the displacement, the following results are obtained from the division of the force by the sections of the samples individually measured. Five samples of each orientation are subjected to the traction test.

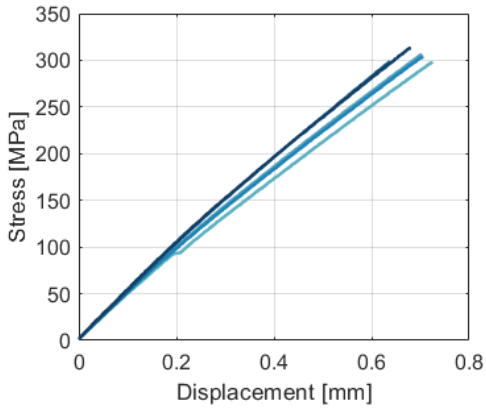

(A) 0°tilt sample.

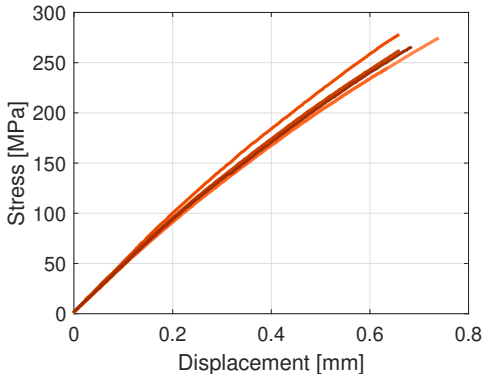

(B) 7°tilt sample.

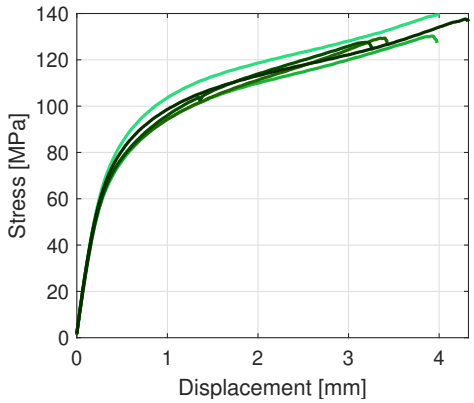

FIGURE 3.4: 45°tilt sample.

The figures show characteristic curves of orthotropic laminates under a traction test with a great difference between the 45° samples and the two others. The curves have a linear behaviour until certain damage is reached probably by the fiber in the 90° directions for the first two orientations. To highlight the variation of the behaviour of the three orientations, a single mean curve is selected for each orientation and superposed in the Figure 3.5.

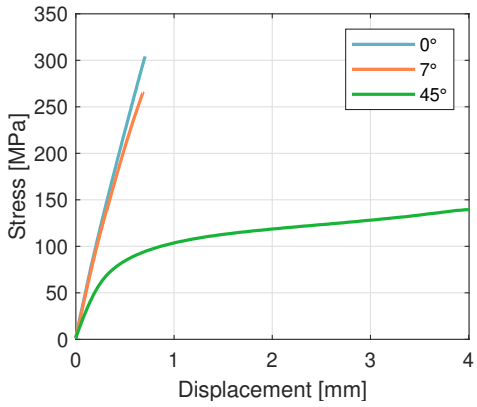

FIGURE 3.5: Comparison between the different plies orientations.

The difference between the 0° and 7° is now visible with a slight tilt downward of the 7° curve. It is clear that the quasi-isotropic hypothesis cannot be validated.

The 0° and 7° samples broke at the fillet in a straight line. The 45° samples, however, broke at the fillet but not straight as it is shown in the next figure. The samples were also whitened under the load. This effect can be seen in Figure 3.6a. The Young modulus of the fabric can be retrieved from the slope of the Figure 3.4a and by dividing the displacement by the total length of the sample.

$$E_{11,22} = \frac{\sigma L}{L_0} = \frac{100x0.05}{0.2} = 25GPa \tag{3.1}$$

This approximation gives a lower value of Young Modulus than the first estimation of 29GPa. A numerical simulation can also help to evaluate the shear modulus as depicted later in the Figure 3.9.

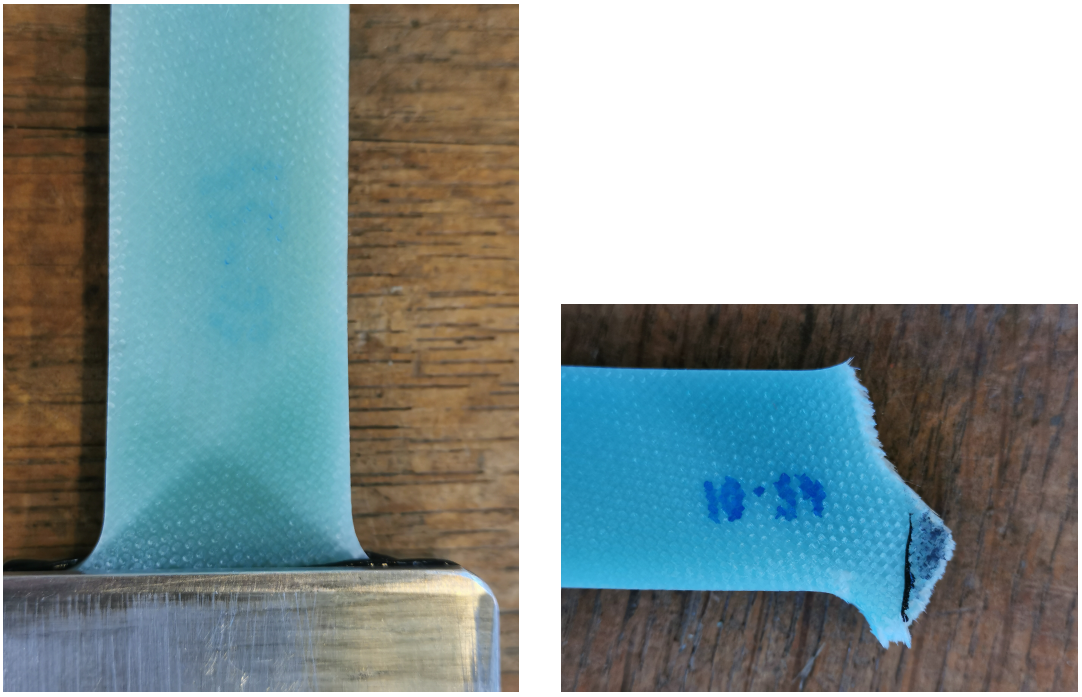

(A) Sample whitening. (B) Sample failure.

FIGURE 3.6: 45°sample after the traction test.

3.3 Numerical analysis

The numerical analysis is modelled using *Nastran* where the composite can be represented using 2D thin shells. The shells contain the laminate stacking sequence and each ply is defined are stated in Equation 2.25 to Equation 2.23 except for the Young modules changed to 25GPa has is it suggested by the analysis of the traction tests.

The first step of this numerical analysis compares the use of 2D and 3D elements to validate the use of 2D thin shells applied to a cantilever beam. Then the model geometry is modified to represent the samples used during the traction and compression tests.

3.3.1 2D mesh validation

The beam geometry is based on the distance between the 300K and 100K stages. This distance is representative of the aperture cylinder height no matter what the final geometry of the structure is. The thickness is based on the samples used for the vibration testing thickness. The dimensions of the beam used to compare 2D and 3D elements simulation are finally: 108x5x5mm.
Both the number of elements along the thickness, $N_{Thickness}$ and along the length, called mesh size, are discussed. The Table 3.1 shows the beam deflections at the lower (d_{up}) and upper surface (d_{down}) using the solid elements. The following scheme shows the different positions of the data retrieved.

Mesh size	$N_{Thickness}$	d_{up}	d_{down}
mm	-	mm	mm
10	1	57,4588	57,456
	2	57,6731	57,6703
	3	57,7281	57,7253
	5	57,7601	57,7573
	10	57,7762	57,7724
5	1	57,9525	57,948
	2	58,0677	57,0632
	3	58,0979	58,0933
	5	58,1162	58,1115
	10	58,1256	58,1209
3	1	58,1309	58,1256
	2	58,2003	58,1946
	3	58,2199	58,2139
	5	58,2329	58,2268
	10	58,2407	58,2345
1	1	58,3198	58,3038
	2	58,3119	58,3048
	3	58,3173	58,3094
	5	58,3243	58,3156
	10	58,3307	58,3216

TABLE 3.1: 3D beam displacement variation with HEXA8 elements dimensions.

The displacement value converges toward the value of 58.33mm. The difference between the upper and lower surface is less than 0.01mm. The use of 2D elements loses this information but gives less than 0.1% of error with less than 5mm mesh size compared to the converging value obtained in Table 3.1. If the type of the elements is CQUAD8, the error is less than 0.1% for all mesh sizes tested.

Mesh size	d_{CQUAD4}	$Error_{CQUAD4}$	d_{CQUAD8}	$Error_{CQUAD8}$
mm	mm	%	mm	%
10	58,2878	-1,49%	58,3464	0,03%
5	58,2878	-0,65%	58,3464	0,03%
3	58,3331	-0,34%	58,3740	0,07%
1	58,3869	-0,02%	58,3858	0,09%

TABLE 3.2: 2D beam displacements variation.

Given the loss differences obtained when comparing solid and thin shell elements, the use of 2D elements to represent the laminate is validated.

3.3.2 Samples numerical model

The numerical model represents an ideal composite and thus, assumptions are made on the laminate. It is assumed that the sample does not contain any damage before the test, with no cracking or air pocket. A single ply is also represented by a perfectly orthotropic material and thus, the matrix, adhesive layer and fibres are not studied separately. The plies are perfectly stuck together, bonded and parallel. No slip appears.

The samples are defined in a 2D plane with shell elements to represent the laminate. The elastic values are defined as stated in 2.3.1 and the stacking sequence is modified to fit the number of plies counted on Figure 2.2. As the traction tests showed great differences between the 0° and 45° oriented samples, the assumption of quasi-isotropy is discarded and each ply is oriented at 0°.

The composite modelling is made using *Siemens NX NASTRAN*. The eight nodes' thin shell elements QUAD8 are selected and after some preliminary simulation, the mesh size for which the displacements converge is 1mm. The boundary conditions are shown in Figure 3.7 with the load and clamping position.

FIGURE 3.7: Boundary condition and position of the load on the sample.

3.3.3 Numerical results

The force applied is 500N and the mesh size is reduced where the thickness of the sample is decreased. The more the mesh size is reduced the more the margin of safety decreases. This behaviour is independent of the material used. Figure 3.8a and 3.8b presents the Tsaï-wu margin of safety of two samples with respectively 0° and 45° plies orientation. The interest of the figures are the distribution of these margin of safeties rather than the absolute values. This highlights the region where the sample is expected to fail.

(A) Tsaï-Wu 0° ply margin of safety.

(B) Tsaï-Wu 45° ply margin of safety.

3.4 Correlation between the numerical and experimental models

The Young modulus is already modified by the analysis of the traction tests. Another simulation with a basic plate of dimension 20x50mm² is done to represent only the small section of the traction samples. The mesh size is kept from the previous numerical model and a load of 100MPa is applied at one side, the other being clamped. Figure 3.9 presents the total displacement computed for two cases: $G_{12} = 4.5$GPa and $G_{12} = 3.8$GPa, both with Young modules $E_{11} = E_{22} = 25$GPa.

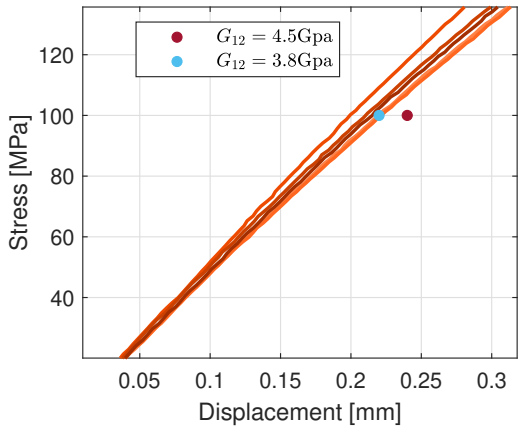

FIGURE 3.9: Correlation between the traction results and the numerical analysis.

The first shear value estimated of 4.5GPa in the material study in chapter 2 already gives a result close to the experimental curve. Decreasing the shear modulus lowers the correlation between the numerical and experimental results. Up to this stage, the correlation showed that the plies were superposed in the same direction. Since the laminate and plies properties do not differ with such a stacking sequence, the plies properties are modified as presented in Table 3.3.

Property	Unit	Value
E_{11}	MPa	25000
E_{22}	MPa	25000
ν_{12}	-	0.12
G_{12}	MPa	4500
$X_{t,c}$ & $Y_{t,c}$	MPa	300
S	MPa	30

TABLE 3.3: 0/90 fabric ply properties reevaluated.

Chapter 4

Current design

4.1 Introduction

As presented in Figure 1.3, the current design selected for the aperture cylinder consists of twelve struts in a z-shape symmetrically distributed around the aperture. The shape is optimised to increase the path between the two stages and thus aims at decreasing the conduction between them. A single strut is holed at each extremity twice to block the rotation. The geometry is shown in Figure 4.1. The thickness is 5mm and the height is 108mm. The plies are oriented with a tilt of 7°with respect to the section, the Y-axis represented in Figure 4.2.

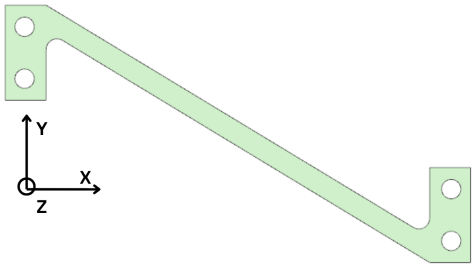

FIGURE 4.1: Current design shape.

The complex shape of the geometry induces high-concentration regions of stress and may decrease significantly the advantages of the composite properties, especially near the fixations holes. The first part of this chapter identifies the weaknesses of the current geometry and performs two small deformations tests based on the strut flexion and bending. A numerical model is created on *Nastran* and reproduces the measures made on the samples. The deformation in the X-axis of the strut can be computed only with a high load. However, the sample shows high deformation with loads along Y-axis and Z-axis. These deformations can be computed for different loads and compared to numerical analysis.

4.2 Numerical model

The shells contain the laminate stacking sequence and each ply is defined are stated in Equation 2.25 to Equation 2.23 with the allowables given by the manufactuer in Table 2.3. A convergence study on the mesh is made on the model in *Nastran*. The four nodes' thin shell elements CQUAD4 are used to mesh the surface. The holes made for bolts are fixed for the six degrees of freedom using 1D connectors with high stiffness on the edge of the bolts holes and the other extremity is subjected to a 500N load as represented in the following figure.

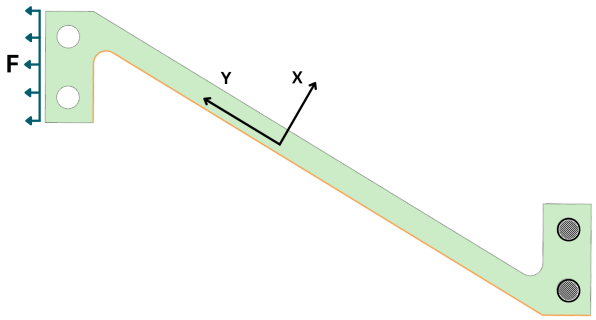

FIGURE 4.2: Boundary condition and load applied for the convergence of model.

First, the stress is evaluated along the strut length. This path is coloured in orange in Figure 4.2. Figure 4.3a shows that the stress does not show any sign of convergence in any location of the path, the smaller the mesh size, the higher the stress values are. The convergence is thus made on the maximal displacement magnitude to avoid the constant increase of the stress concentration zone and converge. The final mesh size selected is 0.3mm.

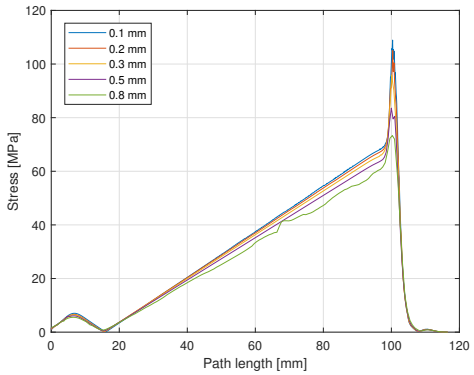

(A) First ply stress distribution along sample path for different mesh sizes.

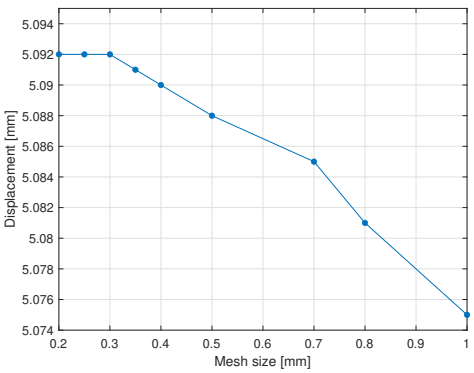

(B) Maximal displacement distribution along sample path for different mesh sizes.

4.3 Testing configuration

4.3.1 In-plane displacements

Figure 4.4 presents the first test setting. It aims at measuring the displacement when the structure is solicited in its plane.

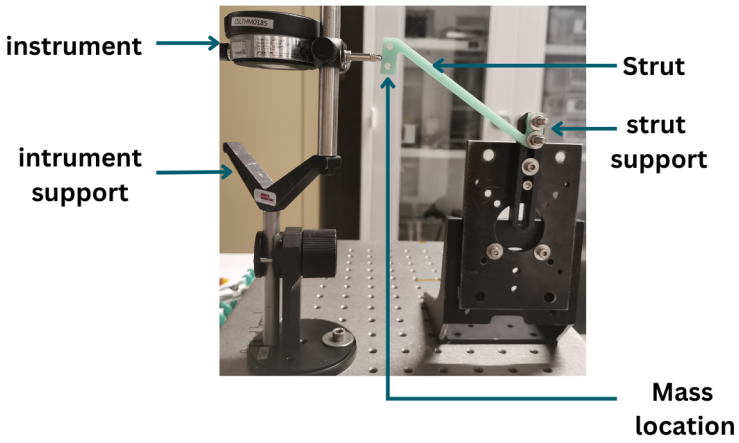

FIGURE 4.4: In plane test configuration.

The sample is fixed at the right extremity on a rigid structure. Vertical displacement is induced by weights placed on the bottom left hole using a chord and a bolt. The different calibrated weights are 100, 200, 500 and 1000g and, using the bolt, the horizontal displacement is measured using a micrometre multiple times. In this way, the repeatability is confirmed and a mean value of displacement can be evaluated. This mean value is computed with ten trials at least and takes into account the weight added by the rope and the bolt measured by a precise balance.
During the measurements, the micrometre is sensible to the composite's irregular and rough surface. Since the measurement is made on small displacements, this imprecision can explain the potential differences with a numerical simulation. The initial position of the instrument is measured to be reproduced in the simulation. The results can be found on the Table 4.1.

Mass	g	108.17	204.16	504.83	1004.17
$\delta d_{measured}$	mm	0.071	0.183	0.572	1.264
$\delta d_{numerical}$	mm	0.102	0.191	0.493	1.05

TABLE 4.1: Horizontal displacement for different vertical loads.

The numerically computed values are retrieved at the same vertical value as the position of the micrometre. The displacement order of magnitude is respected numerically but the values computed are distant from the actual displacements. The young modulus could be slightly decreased to fit better the two last load cases as it is the most influencing value for the present test. However, the tests cannot conclude a precise tendency since for the 100g and 200g weights, the value is overestimated but underestimated for the rest of the predictions.

Stress concentration The current numerical simulation is used to study the stress concentration regions of the strut geometry. During the design process, it is important to be aware of these zones and to reduce or avoid them during further improvement of the geometry. When working with composite, it is even more important to reduce the locations where the fibres are broken such as it is done at the bolt connections holes. The results are displayed in Figure 4.5. The load case studied is the 100g mass case.

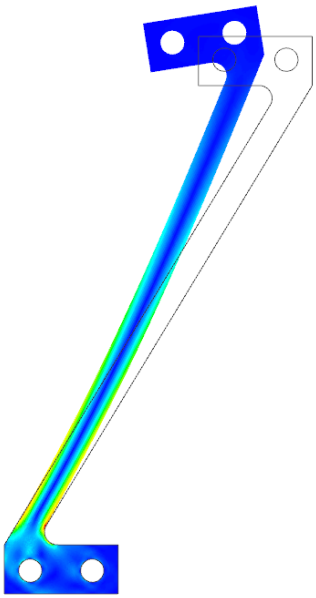

FIGURE 4.5: First ply Von Mises stress (0°angle ply).

The major region of stress results from the rounded edge. The maximal value of stress does not represent the reality since it is highly dependent on the mesh size as shown in the previous section. As all the plies are all oriented in the same direction, the distribution showed in Figure 4.5 remains the same for all. The amplitude computed for each ply also remains equivalent. The reaction forces of the two bolts are balanced.

4.3.2 Out-of-plane displacements

Another test is performed with higher displacement values expected. These test should avoid the errors induced by the surface roughness. The displacement in bending is more sensible to the loads applied.

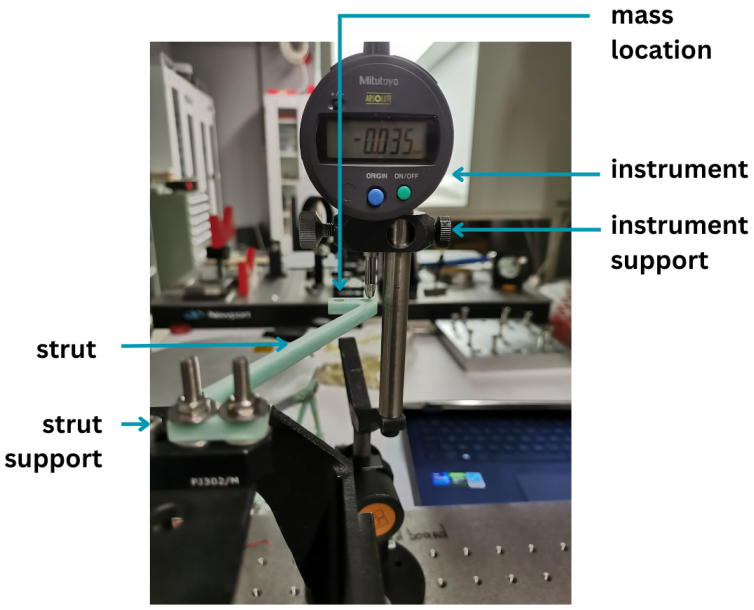

FIGURE 4.6: Out of plane test configuration.

This configuration aims at inducing bending. The sample is thus placed horizontally. Once again, the support structure is built to be rigid and to not induce any displacement when lightly solicited. This time, no bolt is required to ease the measurement. The total weight is thus slightly decreased.
It can be noted that the sensibility to loading in this configuration also increases the impact of the instrument on the result. Indeed, a small displacement can be seen with bare eyes when the instrument is placed on the surface of the sample. This might induce a small error, especially for the first tested weight .
The results are displayed in Table 4.2.

Mass	g	104.80	200.79	501.46	1000.8
$\delta d_{measured}$	mm	0.35	0.77	1.81	4.17
$\delta d_{numerical}$	mm	0.32	0.61	1.56	/
$\delta d_{E_{11,22}=25GPa,num}$	mm	0.33	0.63	1.57	/
$\delta d_{E_{11,22}=22GPa,num}$	mm	0.37	0.71	1.75	/

TABLE 4.2: Vertical displacement for different vertical loads.

The values measured with the 1kg weight are discarded from the study as the displacement increased continuously during the experiment. As the amplitude grows with time and is much higher than the other amplitudes, the assumption of small displacement is not respected.
The first three results are kept and show a clear tendency to start a correlation. By decreasing the Young modulus from 29000 MPa to 22000 MPa, the results get closer to the actual displacements of the all the load case.

Stress concentration The same study is made as it is done for the first test. The graphical distribution of Von Mises stress is displayed in Figure 4.7a. The stress concentrates once again at the bottom fillet. The stress distribution is uniform along the section. As all the plies have the same orientation, the distribution remains the same for each ply. The amplitude of the Von Mises stress however, changes for each ply and the mean stress value of the whole piece is presented in Figure 4.7b

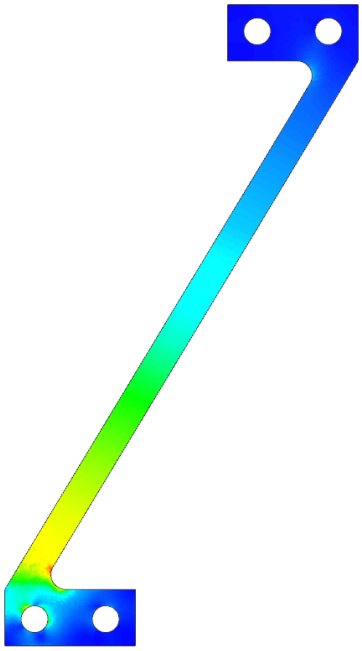

(A) First ply Von Mises stress (0°angle ply).

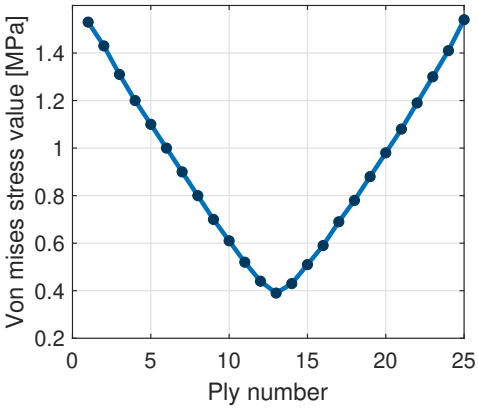

(B) Plies average Von Mises stress values.

FIGURE 4.7: Stress distribution analysis under bending with a 100g mass.

4.4 Conclusion

During the numerical analysis of the current strut shapes, the fillets appeared as the most probable zone of failure for both the bending and flexion tests. The addition of the fillet decreases the stress concentration at the top and bottom of the strut. The fillet radius could be studied to decrease even more the stress concentration with in mind the addition of thermal conduction if the radius is increased. This study is made in chapter 6.
The bending tests were expected to show significant displacements and confirm that the critical load cases of this design are out-of-plane forces induced. The stress distribution shows that the first ply is more likely to fail first.

Chapter 5

Vibration testing

5.1 Introduction

The aperture cylinder is subjected to multiple requirements stated in chapter 2. The scope of this chapter is the study of two of these requirements and the correlation between the numerical model and the experimentation made using vibration testing.

The first requirement is a frequency of the first significant mode above 150Hz. Ideally, the first frequency of the model should overcome this threshold to provide enough security with the mission design requirement and thus, not amplify the own resonance frequencies of the structure on which the ApC is mounted: the cryostat. As it is seen through this chapter, the composite reduces the eigenfrequencies in comparison with the frequencies of the same structure made of metal but the use of metal is discarded is chapter 2 since the allowed quantity of material to validate the thermal requirement tends to 0.
The second requirement is the capacity to sustain the loads expected during the life of the mission. The most critical part is the launch. As the outer vessel level is limited to 25g as explained in *Athena XIFU - Aperture Cylinder Design Description* [2], a vibration test is performed with a maximal acceleration of 25g and the structure is then checked to locate potential damage.

On a second basis, the vibration test provides a comparison between the dynamic behaviour of the structure numerically predicted and what is observed when the structure is physically excited. This process aims at validating the numerical model and, if required, at proceeding with a correlation between the model and the experimental results. This last part required spotting the differences and similarities between the two sets of data to then, identify and locate the sources of discrepancies between them. Finally, adjustments are based either on the model connections and assembly or directly on the material properties.

To evaluate these requirements, vibration testing is performed on a structure made using the selected composite. A shaker is used to control the vibration and various tests are made to assess the behaviour of the structure, in terms of frequencies and displacements. The tests, however, are not made to retrieve the structure mode shapes. On the other hand, the numerical representation of the structure is intensively studied through boundary conditions influence and mesh convergence analysis.

5.2 Numerical analysis

In the following pages, a numerical model is built and analysed extensively to represent the real structure used for the vibration testing as precisely as possible. The precision of such a model is essential to design a sub-system as it is used as a first estimation of whether a design is suitable or not for the current application. If the numerical model validates the required specificity of the structure, a real model is built and tested.
The numerical model aims at simplifying the reality of the whole telescope structure but also the complex CAD made by *GDTech* showed in Figure 1.3. The mass supported by the aperture cylinder being known, and the 100K flange being considered as relatively stiff, this flange can be approximated by a lumped mass equivalent of the real flange mass of around 1.3kg.

The geometry is presented, the elements and mesh sizes selected are defined and the connections between the struts and the 100K stage are discussed. The boundary conditions influence is analysed as well as the properties of the connections.

5.2.1 Modelisation

The structure built is composed of twelve struts tightened to the baseplate and the first stage by screws. The latter is a dodecagon with 12.5mm of thickness and a 60.56mm distance between two adjacent edges. Figure 5.1 presents the model used during the vibration tests.

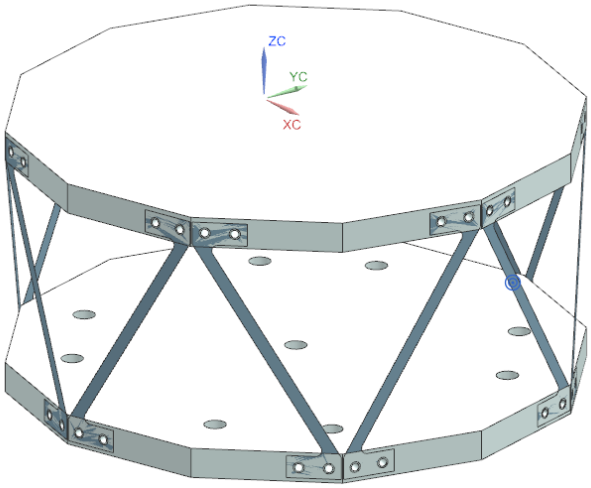

FIGURE 5.1: Setup designed for vibration testing.

The numerical model is represented without the lower floor as it is fixed to the shaker interface to prevent any movement from it. The 100K stage is made out of aluminium 6061 and weighs 1.37kg. With the geometry and assembly now defined, the structure mesh is now studied for both the upper base and the struts. The links between the different parts are also defined.

5.2.2 Mesh

Connections

In reality, the struts and stages are assembled using screws. To reduce the computational time of the model, these screws are represented by 1D rigid elements *RBE3*. The *RBE3* elements transmit the load between the mesh elements connected without adding stiffness. However, its single dependent node, the central node, cannot be linked to another rigid body element directly. An intermediate stiff element is added between the dependent nodes of the RBE element: *CBUSH*.

The latter connects multiple rigid elements, and when coincident, does not contain any rotational free-body mechanisms. The stiffness terms of the connector are defined manually by the user and add this stiffness directly to the stiffness matrix. A stiffness value too high will induce an early termination of the simulation as the stiffness matrix will be ill-conditioned while a too-low value will not represent correctly the rigidity of the screw.

The mesh around the strut holes is linked to a central node. For the upper joints, another central node is linked to the whole interior surface of the 100K stage holes. The two central nodes are finally linked together using a *CBUSH*. Figure 5.2 shows the results obtained. The rigid elements connecting the strut elements (blue) are linked to the ones connecting the screws hole (green) with a *CBUSH* connector not visible as the independent nodes of the two sets are coincident.

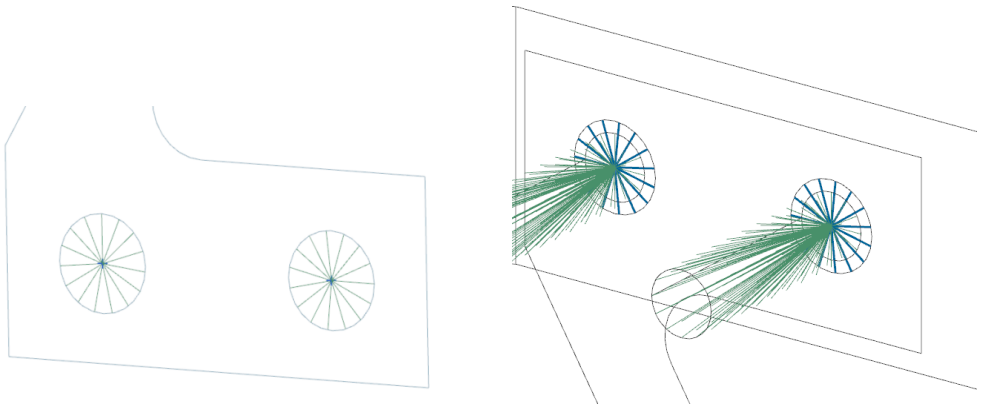

(A) Lower part. (B) Upper part.

FIGURE 5.2: screw representation using rigid elements.

A sensibility study is performed on the *CBUSH* connectors stiffness values. A lower value is preferred to avoid high ratios in the stiffness matrix, but a higher value is physically more representative of reality. Between 10^{16} and 10^{10} N/mm, no significant variation in the frequencies is noticed. A 10^{7} N/mm stiffness decreases the frequency by 1Hz. When comparing the FRF of the 10^{15} and 10^{7} stiffnesses, the amplitude variation can be neglected. The first peak amplitude difference is less than 0.01. With higher stiffness, the simulation cannot proceed. Lower values however reduce too much the structure stiffness and thus, the frequencies suddenly drop to lower values. The stiffness value selected is 10^{8} N/mm. This order of magnitude can

be compared with a computation on the screw stiffness by the equation Equation 5.1.

$$k_{trans} = \frac{EA}{L} = \frac{210\ 10^9 x \pi 0.00165^2}{0.011}\ 1.6\ 10^8 \tag{5.1}$$

The same study is performed on the torque values and a stiffness of 10^5 N.mm is retained for the three rotation directions.

Mesh convergence

The mesh convergence was already made on the stress for the 2D thin shells representing the struts. The convergence is now made based on the first eigenfrequency. Then the same process is applied to the 3D elements used to represent the upper stage.

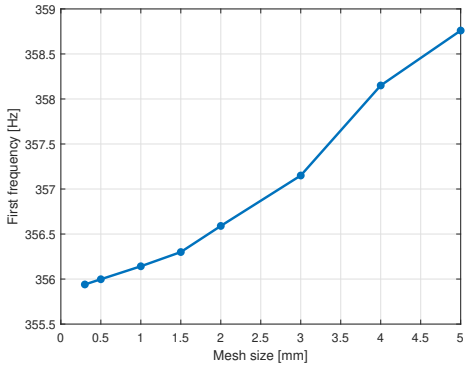

(A) First eigenfrequency variation with CQUAD4 mesh sizes for CTRETA4 of 3mm.

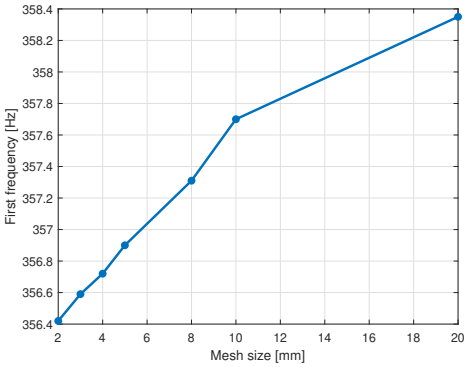

(B) First eigenfrequency variation with CTRETA4 mesh sizes for CQUAD4 of 0.2mm.

It can be noted that below a 2mm size for the solid mesh, the simulation presents memory issues and the simulation does not end. The mesh sizes are selected to obtain a minimal difference of 1Hz with the most refined mesh. The thin shell elements size is 3mm and the solid elements size is 5mm. In comparison, the mesh size convergence in chapter 4 reduced the struts 2D mesh to 0.3mm which highlights the interest of a study based on the structure's frequencies.

5.2.3 Boundary conditions

Realistic boundary conditions are crucial for a realistic analysis of a dynamic simulation. The structure behaviour is greatly affected by the boundary conditions. The present section aims at understanding the impact of the boundary conditions on the eigenfrequencies and thus its sensibility to different ways to define the shaker configuration.

Six different cases are studied. The first case fixes the translation of the contour of the holes, the second case also constrains the rotational degrees of freedom. The next two cases, also restrain the same degrees of freedom but on the independent nodes of rigid body elements built around the edge of the holes. The cases 5 and 6 aim at creating a boundary condition between cases 3 and 4. In this case, the edge for case

6, or central node for case 5, is still fixed in translation but only two rotations axis are fixed. The rotational boundary conditions are created based on the cylindrical coordinates of each hole and free only the rotation around the Z-axis of the cylinders. This boundary conditions represent with more accuracy a simplified version of the screwed connections.

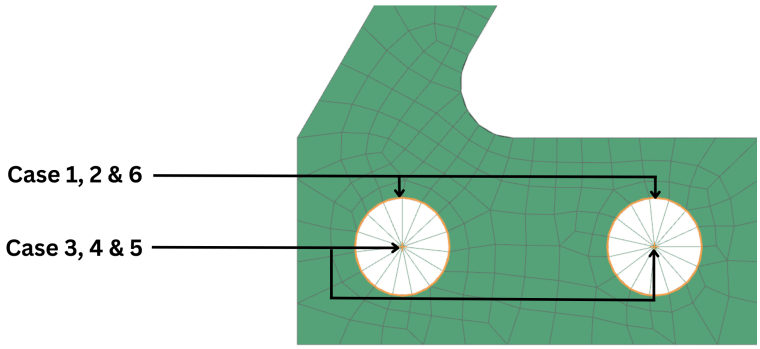

FIGURE 5.4: Boundary conditions locations.

The first three frequencies are computed for each case and are displayed in the following table.

Mode [Hz] / Case	1	2	3
1: Fixed translation and rotation of edge	358.63	688.05	724.44
2: Fixed translation of edge	358.58	688.04	724.43
3: Fixed translation and rotation of central node	356.30	685.54	719.69
4: Fixed translation of central node	347.56	678.49	704.21
5: Free rotation in cylinder axis at edge	349.35	678.91	704.25
6: Free rotation in cylinder axis at central node	349.28	678.89	704.25

TABLE 5.1: Boundary conditions influence on the three first eigenfrequencies.

5 of the boundary conditions do not influence the first four modes' shape. The case 4, however, changes the behaviour of the struts by adding bending displacement in higher frequencies. Case number 5 modes show the same mode shapes as mode 3 but its eigenfrequencies are closer to the ones found constraining only the translations. Case number 6 is very similar to case number 5.
It can be noted that the first frequency is more sensitive to the specificity of cases 5 and 6 when compared to case 4. This behaviour is attributed to the shape of the first mode that induces a rotation out of the plane for certain struts. Figure Figure 5.5 presents the different modes shapes.

Finally, case number 5 is selected to describe the boundary conditions as the rotation is possible in the screw axis only, represents better the reality and does not over-constrain the model as case number 3 does.

5.2.4 Modal response

Now that the model is studied, the modal response of the structure can be analysed. This section shows the frequency values and shapes of the modes numerically computed. After that, a brief discussion on the accelerometers location is suggested from the mode shapes. As the chapter 4 showed, the quasi-isotropic assumption on the laminate stacking sequence do not fit the results obtained during the traction tests. In consequence, the results of the numerical analysis presented and compared with the experimental tests are obtained using a stacking sequence with plies at 0°.

Eigenfrequencies

The resonance frequencies between 0 and 2000Hz are displayed on the Table 5.2. The first mode value is higher than the 150Hz required and a lot of frequencies are very close with each other. This is caused by the symmetry of the structure and the struts disposition. Figure 5.5 presents in the next paragraph the first modes. The majority of the modes after mode 6 are mainly driven by the struts displacements. As the struts represent a small proportion of the total mass, it explains the low mass proportion found in the Table 5.2.
The effective modal mass ratio is evaluated for each mode and the sum approaching the 100% is presented.

# Mode	Frequency	$\%X_{Mass}$	$\%Y_{Mass}$	$\%Z_{Mass}$	$\%RX_{Mass}$	$\%RY_{Mass}$	$\%RZ_{Mass}$
1	359	7.76	87.59	0	74.40	6.59	0
2	359	87.70	7.75	0	6.59	74.41	0
3	693	0	0	92.08	0	0	0
4	726	0	0	0	0	0	93.35
5	1084	0.68	0.03	0	0.71	16.13	0
6	1085	0.03	0.68	0	16.12	0.71	0
7	1085	0	0	0	0	0	0
8	1085	0	0	0	0	0	0
9	1085	0	0	0.12	0	0	0
10	1086	0	0	0	0	0	0
11	1086	0	0	0	0	0	0
12	1086	0	0	0	0	0	0
13	1086	0	0	0	0	0	0.0
14	1086	0.04	0.06	0	0	0	0
15	1087	0.06	0.04				0
16	1087	0	0	0	0	0	0.04
17	1138	0.11	0.07	0			0
18	1139	0.07	0.11	0			0
19	1692	0	0	0	0	0	0
20	1692	0	0	0	0	0	0
21	1741	0	0	0	0	0	0
22	1753		0.01	0.05	0	0.01	0.00114
23	1753	0	0	0	0	0	0
24	1754	0		0.02	0	0	0
25	1754	0	0	0.22	0	0	0
26	1755	0.05	0	0.01	0.01	0.02240	0
27	1756	0.07	0.07	0	0.02	0.02270	0
28	1757	0.03	0	0	0.01	0.00271	0
29	1758	0	0.01	0	0	0.01	0
30	1767	0	0	0	0	0	0.37
31	1833	0	0	0	0	0	0
32	1835	0	0	0	0	0	0
	TOTAL	96.97	96.42	92.36	97.85	97.85	93.51

TABLE 5.2: modal effective masses and inertia (>5% highlighted).

Mode shapes

Figure 5.5 displays the first modes shapes. The structure behaviour, especially for the first frequencies, is used to evaluate the ideal position of the accelerometers of the strut during the experiment in a shaker.
In Figure 5.5a, the plate moves along the X-axis. the second is a symmetrical representation of the first mode. In reality, this mode can be found for each plane of symmetry of the structure. The third mode is driven by an up-and-down displacement of the plate and the fourth one is a rotation around the Z-axis while the fifth mode is a rotation around the X-axis of the plate. The rest of the eigenfrequencies are mainly driven by the strut displacements and only one mode showing this kind of behaviour is displayed here.

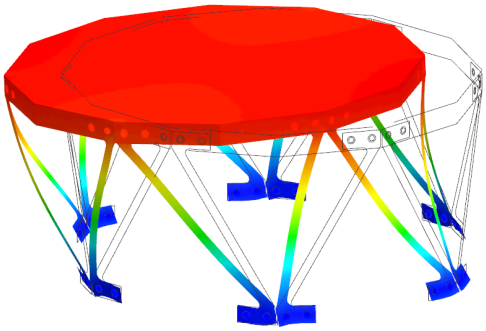

(A) First mode, f = 359 Hz.

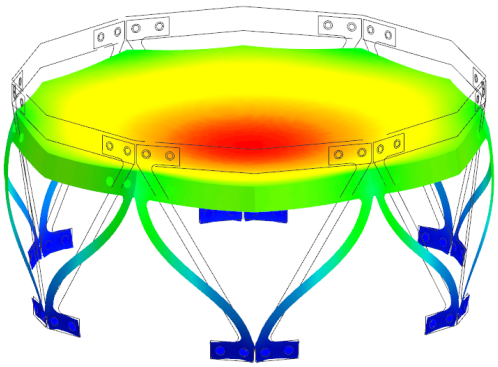

(B) Third mode, f = 693 Hz.

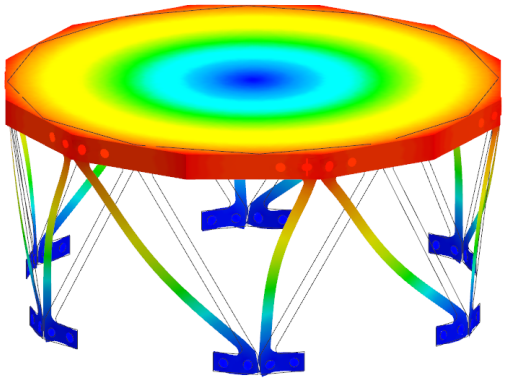

(C) fourth mode, f = 726 Hz.

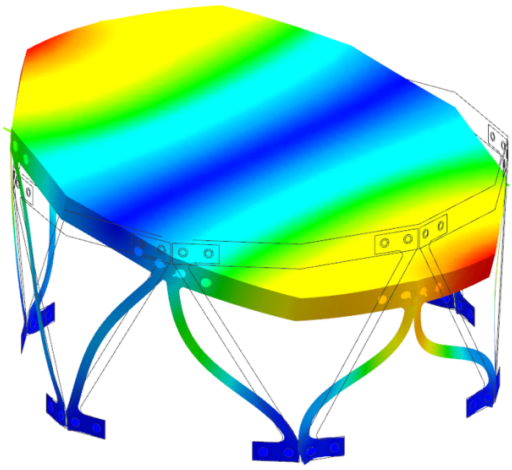

(D) Fifth mode, f = 1084 Hz.

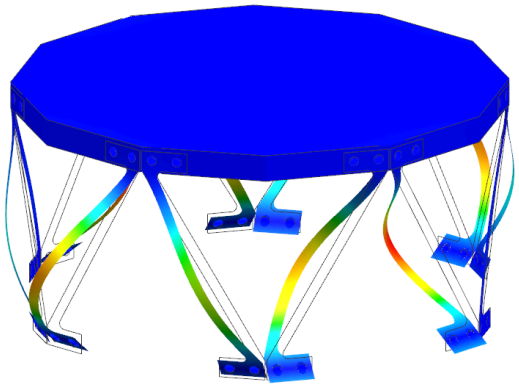

(E) Seventh mode, f = 1085 Hz.

FIGURE 5.5: First modes shapes numerically computed.

Accelerometers position discussion

The modes 1 to 4 in Table 5.2 are based on the aluminium plate displacement, in rotation or translation. The accelerometers can be placed near the extremity of this plate. Since there is enough space for multiple accelerometers, two of them can be placed on the X and Y-axis and one at the centre of the ring. This last accelerometer is expected to be more excited at frequencies near the third mode as the centre shows the higher displacements values in Figure 5.5b but less excited by higher modes as either the centre or the whole plate is not predicted to show high displacement. The struts section does not provide enough space in reality to glue an accelerometer. The three ideal positions are shown on the Figure 5.6.

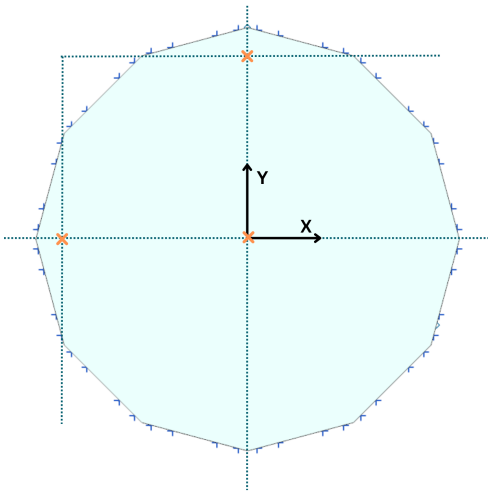

FIGURE 5.6: Proposition of location for three accelerometers based on the numerical modes computed.

5.2.5 Dynamic response

The vibration testing on a shaker is reproduced for both vertical and horizontal excitation. The dynamic response analysis shows the different eigenfrequencies of the structure that will be later on compared with the response measured during the experimental testing. It also shows the shape of the mode encountered. The experimental setup such as the positioning of the accelerometers can be helped by knowing the expected modes shapes. The damping factors are then discussed and a random vibration excitation is performed on the structure. The accelerations at different locations are retrieved and the data is used to compute the PSD and the corresponding FRF. The computations are made using a viscous damping of 1% applied to all the modes for now. This expected damping value is retrieved from Berthelot et al. [3] in the case of serge glass epoxy laminate.

Input excitation

The PSD evaluation requires first setting the input PSD acceleration used by the solver. This function is defined based on the test in the shaker input definition as stated in Table 5.3. This input PSD defines the distribution of power over the frequency range of excitation defined between 20 and 2000Hz.

Frequency	Input
Hz	g^2/Hz
20	0.00881
100	0.0439
300	0.0441
2000	0.00189

TABLE 5.3: PSD G acceleration input.

Data location sensibility

Now that the excitation direction and amplitude are
defined, the PSD can be computed and then transformed into an FRF to be compared with the experimental results. The location of the response point is important in the process of numerical model validation. The mesh nodes cannot correspond exactly with the accelerometers' position during the experiments. Thus, the data sensibility is evaluated in this section. Three different positions are taken: one at the closest node to the ideal position of one of the accelerometers as shown in Figure 5.6 and two at very close locations.

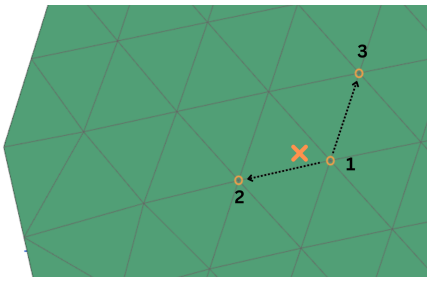

FIGURE 5.7: Measurement locations around the ideal position of the accelerometer in the X-axis.

The three curves are superposed in an FRF graph for both vertical and horizontal shaking directions. In the vertical direction, the FRF amplitude at the first peak is decreased as the reference node approaches the edge of the structure. The difference between locations 3 and 2 at the peak is 15.52 in FRF which represents approximately 15% of the amplitudes. The tendency is reversed for the high frequencies. The difference between the different nodes are easily understood by the shape of each mode. The third mode induces higher displacement at the centre of the 100K stage. For the horizontal displacement, no differences in amplitude can be noticed for the first node peak. The same conclusions are made for the central and Y-axis accelerometer.

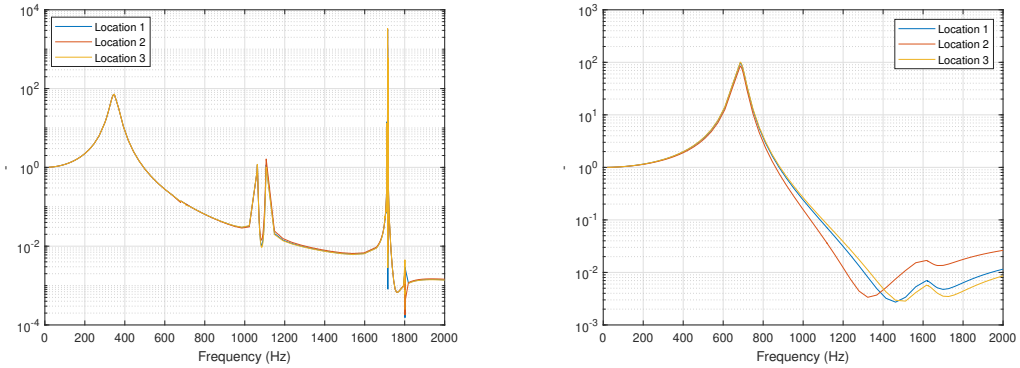

(A) Horizontal excitation.

(B) Vertical excitation.

FIGURE 5.8: Frequency response function at three locations around the ideal accelerometer position

5.3 Vibration testing on a shaker

This section introduces vibration tests performed on the designed structure. The setting is first discussed and shown. Two vibration directions are tested, one in the horizontal plane and one in the vertical plane. For both directions, multiple vibration tests are performed with either sine swept or random signals. The results are compared and analysed using the PSD and FRF of the different tests.

5.3.1 Experimental setup

The structure is mounted on the interface plate of the shaker with a baseplate. Nine fixations connect the 300K flange of the structure and the intermediate baseplate to ensure that they don't influence the results. Three accelerometers are placed according to the nodes selected in Figure 5.6 on the 100K flange and two controllers are stuck for redundancy to the 300K flange. Each strut is numbered to be differentiated in case of failure or damage during the test. A marker indicates the screw position before the tests. These marks are checked after each test to detect a potential defect during the clamping. The potential damage is also investigated visually between two vibration tests. The horizontal shaking direction is tested first and only the intermediate plate is dismounted to change the direction to the vertical axis. Figure 5.11 and Figure 5.13 present the two configurations.

M1 refers to the central accelerometer, M2 and M3 and the ones placed respectively in the X and Y axis as depicted in Figure 5.6. Controller C1 is along the Y-axis and controller C2 is along the X-axis. It can be seen from the picture that the used accelerometers would have been indeed too wide to be placed on a strut as suggested during the accelerometers location discussion.

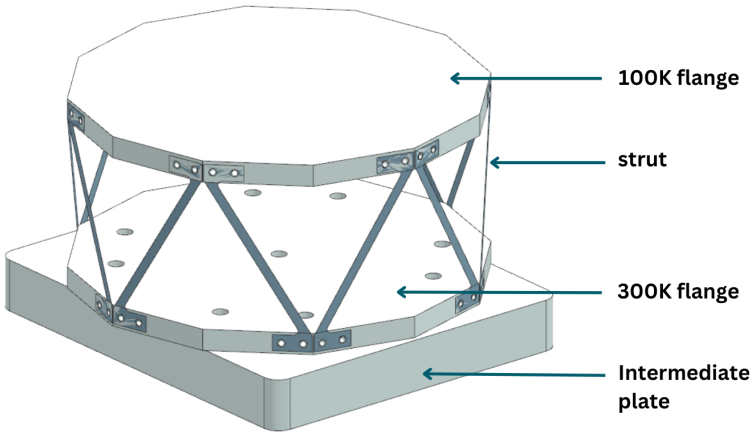

FIGURE 5.9: 3D model of the structure used during the vibration tests on the shaker.

Horizontal configuration

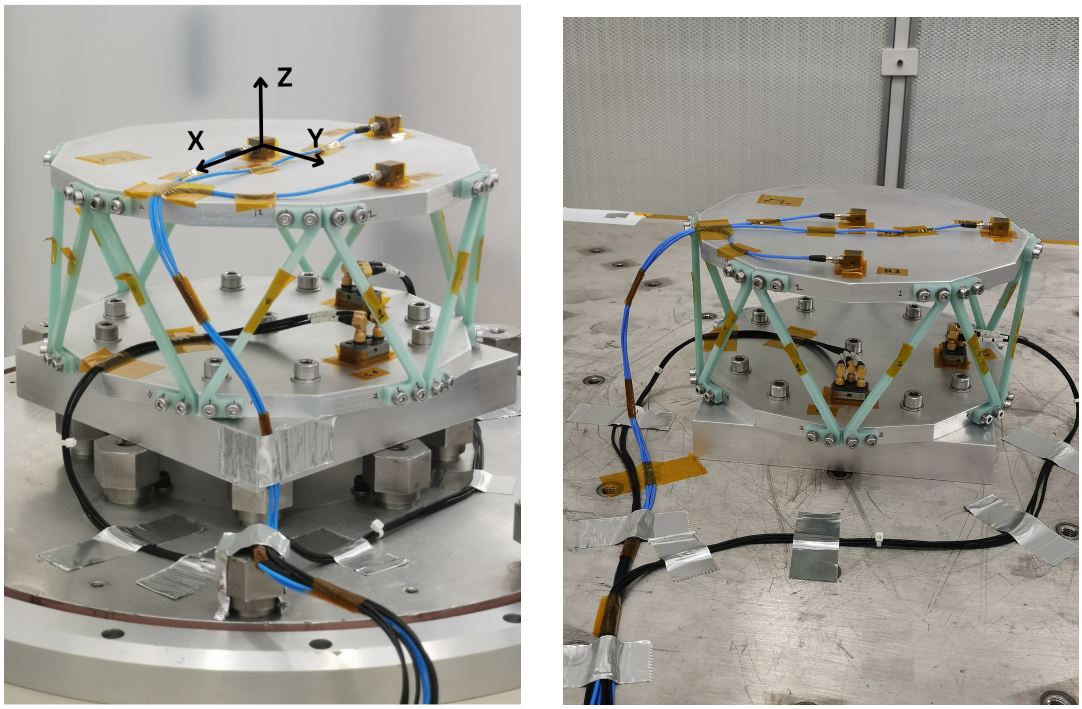

FIGURE 5.11: Horizontal configuration on the shaker.

Vertical configuration

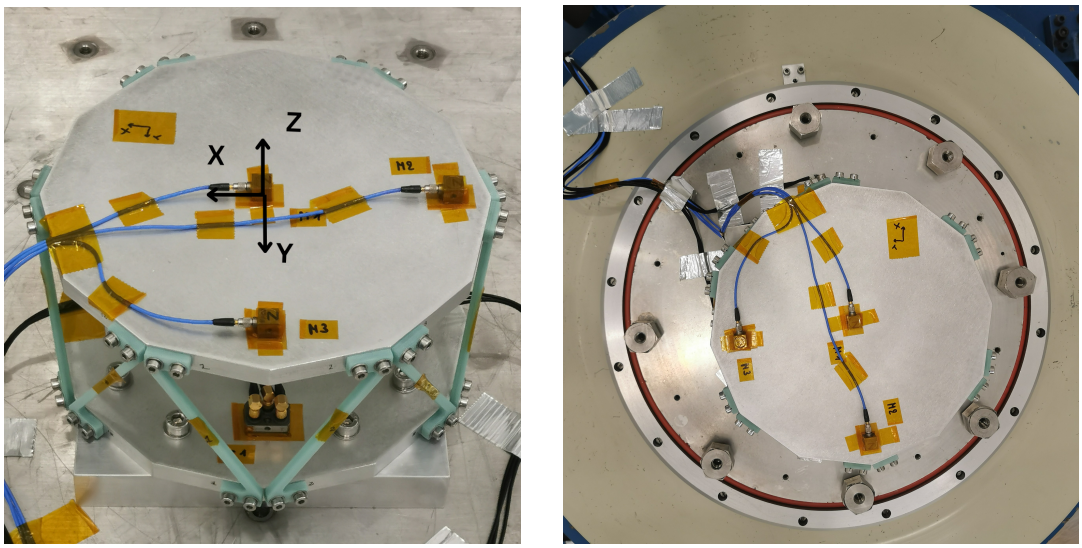

FIGURE 5.13: Vertical configuration on the shaker.

5.3.2 Experimental results analysis

Multiple tests are performed on the structure for both axes tested. The acceleration at each measurement instrument location is retrieved and graphically represented for each frequency transmitted by the shaker. This graph represents the PSD of the test. By dividing, the PSD values by the acceleration measures by the controllers, the frequency response function is obtained. The FRF function is a transfer function expressed in the frequency domain and thus expresses the structural response to the external forces applied by the shaker.

The first test is a sine sweep and quickly covers all the frequencies between 5 and 2000Hz to spot the peak of resonances. The sine sweep test has an acceleration of 0.5g in input with a sweep rate of 2 Oct/min.
The random tests are then performed with values of -9, -6 and -3db for the horizontal test. The vertical configuration random tests have levels of -12, -9 and -6db. The structure gives high displacements at -6db in the vertical configuration and thus, the test was not performed at -3db.
In between all the random tests, a sine sweep is done on the structure and the corresponding FRF curve is superposed with the ones already performed during the previous sine sweep. This indicates if the random test modified the structure and thus modified its response to the input. This modification could result from damage inside the material or the screw loosening for example. The test did not show such behaviour and all the tests were performed without any incident.

The first test analysed is performed using a sine sweep. Compared to a random input, the FRF curve is smoother and makes it easier to spot the eigenfrequencies.

The data is shown for the three accelerometers. Only the X-direction is kept for the horizontal test and the Z-direction for the vertical test. As expected, the first mode is excited by the horizontal test and the second one by the vertical one. The values found at the peaks are displayed on the Figure 5.14.

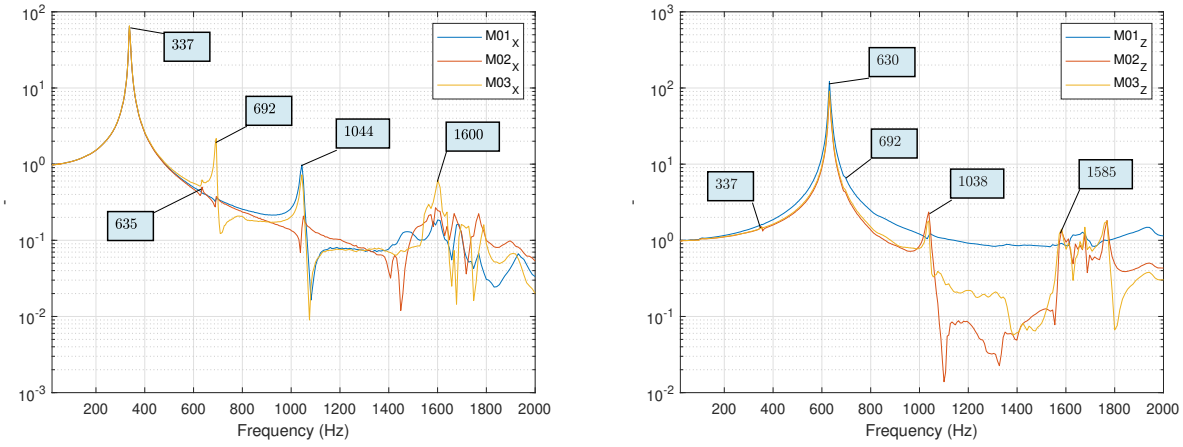

(A) Horizontal axis.

(B) Vertical axis.

FIGURE 5.14: Experimental FRF for sine test.

Viscous damping

Peak picking method (PPM) Now that the resonance frequencies are retrieved, the method of peak picking can be used to study one of the frequencies. This method will be applied to the first mode only.

The peak-picking method is used if the peak is well enough defined and not overlapped by another close resonance frequency. This method is thus a single input single output (SISO) and a single degree of freedom (SDOF) method. The peak-picking method is considered the simplest method to estimate modal parameters in the frequency domain. These parameters are the natural frequency, their respective damping factors and residues.

This method is applied on the most prominent peak found in Figure 5.14 which is the mode at 337Hz for the horizontal vibration test and the 630Hz for the vertical test. The two modes validate the SDOF requirements.

As the instrument provides data points, the curves are not continuous and thus imprecise, especially around resonance frequencies. The data is thus refined around the peak by interpolation inside the window chosen.

With the data interpolated, the resonance frequency is evaluated as well as the frequencies on the half-power points f_a and f_b, which are defined by an amplitude worth $|\hat{\alpha}|/\sqrt{2}$ where $|\hat{\alpha}|$ is the amplitude of the resonance frequency. From there, it is possible to retrieve the quality factor and the damping ratio using the following equations:

$$f_r = max(FRF), \tag{5.2}$$
$$\Delta f = |f_a - f_b|, \tag{5.3}$$
$$\zeta_1 = \frac{\Delta f}{2 f_r}, \tag{5.4}$$
$$Q = \frac{f_r}{\Delta f}. \tag{5.5}$$

The damping values found by averaging the result of the peak-picking method on all the sine tests performed for modes 1 and 2 are 0.83% and 0.46% using the accelerometer 2 in X for the first mode and Z directions for the second mode.

The accuracy of the peak-picking method highly depends on the frequency resolution as it defines the values of f_a and f_b but also on the validity of the SDOF assumption. This method has shortcomings from this assumption and contains a lot of uncertainties, especially for lightly damped structures as it is the case for the modes studied. Indeed, the data rate might miss the real peak and thus, the damping factor can be overestimated.

Three random tests are presented here -9,-6 and -3db in the horizontal solicitation and three other tests at -12, -9 and -6 db for the vertical configuration.

Random test on X-axis at -9db

Figure 5.15 shows the PSD of the random vibration test made at -9 db. The input is the same as referred to in Table 5.3. It shows the difference between the three accelerometers' data retrieved in the X directions.

The Y-axis accelerometer M03 shows large amplitudes compared to the other two accelerometers around 680Hz. The MO1 accelerometer does not show a clear increase in amplitude around 1030Hz as the MO2 and MO3 do.

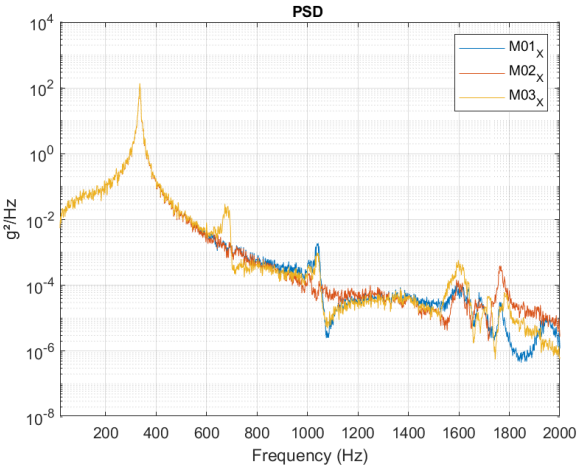

FIGURE 5.15: PSD of all accelerometers in X-axis for -9db random test in X-axis.

Random test on X-axis at -9db, -6db and -3db

A comparison between the different levels tested is made on the graph using the central accelerometer as an instrument of measure, still in the X direction.
As it is expected, the curve increases the higher the value of decibels is. The RMS is computed for the three tests: 32.78, 41.04 and 51.54 gRMS. The damping factor associated with the three tests are 0.43, 0.61 and 0.88% and thus, the damping ratio and output RMS value increase as the input RMS value increases too.

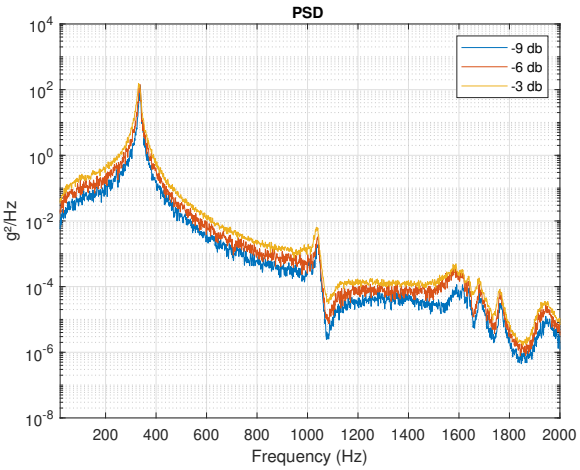

FIGURE 5.16: PSD of central accelerometer in X-axis for -9db, -6bd and -3bd random test in X-axis.

Random test on Z-axis at -12db

Figure 5.17 shows the PSD of the random vibration test made at -12 db on the vertical axis. the graph shows the difference between the three accelerometers' data retrieved in the Z-direction.

The MO1 accelerometer does not show a clear increase in amplitude around 1030Hz as the MO2 and MO3 do just as it was already the case for the horizontal test.

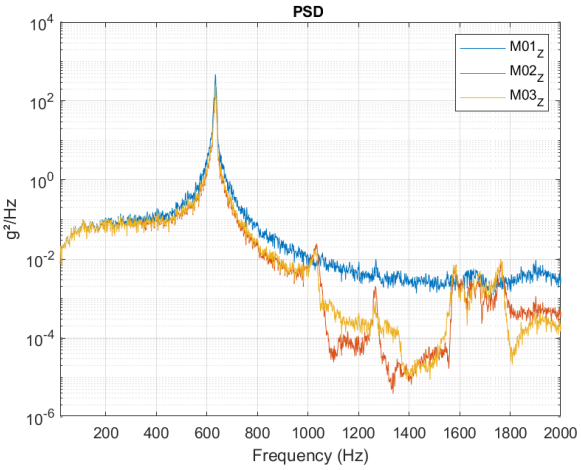

FIGURE 5.17: PSD of all accelerometers in Z-axis for -12db random test in Z-axis.

Random test on Z-axis at -12db, -9db and -6db

Figure 5.18 presents a comparison between the different levels tested using the central accelerometer as an instrument of measure, still in the Z direction. As this accelerometer shows the highest amplitude in the previous graph, its study gives insights into the worst-case scenario.
As it is expected, the curve increases with the value of decibels. The gRMS are computed for the three tests: 60.0, 81.7 and 100.0 gRMS. These values are much greater than their equivalent decibels in vertical excitation. The damping value however only slightly varies with 0.47, 0.32 and 0.39% which doesn't give a clear tendency.

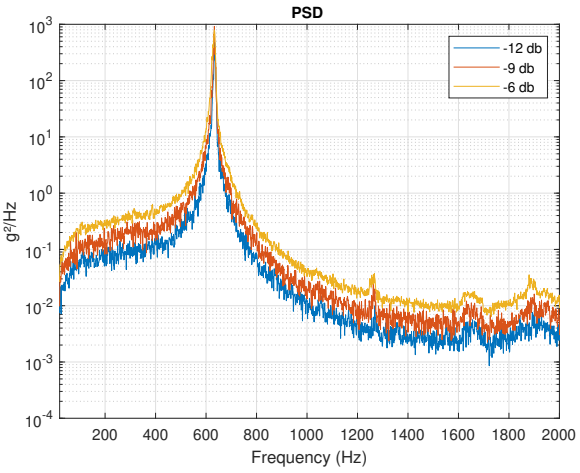

FIGURE 5.18: PSD of central accelerometer in Z-axis for -12db, -9db and -6db random test in Z-axis.

RMS Extrapolation

An extrapolation of the RMS is evaluated for both the vertical and the horizontal vibration tests. This extrapolation formulates the property according to which, a decrease of 6bd divides by 2 the RMS value. The curve is placed to minimze the error with the measured values.
At -9db, when the vertical axis of the structure is excited, the response shows an amplitude of RMS more than twice the values found when a vertical excitation is performed. If the structure was excited with -3db such as it is done with the horizontal configuration, an RMS value of around 155gRMS would be expected.

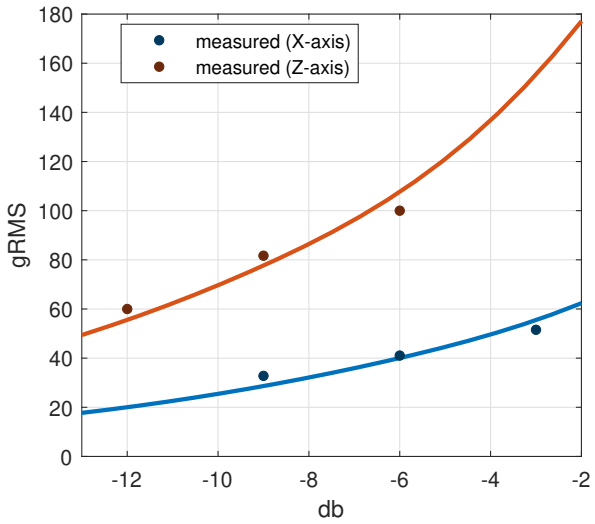

FIGURE 5.19: RMS values measured and corresponding extrapolations for vertical (red) and horizontal (blue) vibration tests.

5.4 Correlation with tests

The correlation is based on two objectives. The first one is to fit the amplitude of the FRF computed numerically and experimentally. The second one is to adapt the material properties in the numerical model to obtain the same first frequency value as the one found experimentally. The other frequencies found are also discussed during the process of correlation.

The experimental vibration testing provided numerous data sets which can be used to proceed with the correlation. The sine-swept test is discarded for this part because the numerical analysis can only be made on random vibration. Three random tests were done for each configuration. The correlation is only made on the lowest decibel level for each configuration. To do so, the input excitation is set the same as used during the experiments.
The inputs for the horizontal excitation are already used for the sensibility study and are shown in Table 5.3, and the inputs used for the -12 db in the vertical configuration are shown in Table 5.4. Finally, the study is based on the second accelerometer data.

Frequency	Input
Hz	g^2/Hz
20	0.01070
100	0.0530
300	0.0530
2000	0.00227

TABLE 5.4: input excitation function.

First, the damping coefficient is correlated. As suggested in Berthelot et al. [3] for serge laminate of glass epoxy, the first frequency damping value expected is 1%. The damping is evaluated for both the first and second frequencies' peak actual damping using the peak-to-peak method applied to the random tests at the lowest levels in X (-9db) and Z-axis (-12db). This method gives for the first peak a damping value of 0.48% and for the second one a value of 0.46%.
The damping values found to correlate with the experimental FRF are 0.8 and 0.4%.

The damping value found for the X-axis vibration test is very close to the 0.8% found in Berthelot et al. [3] for serge laminate frequency around 300Hz but double the damping value of 0.43 found using the peak-to-peak method. On the other hand, the damping value around 0.4% of the Z-axis vibration test is half the reference value of 0.8%. Finally, Figure A.3 presents the superposition of the experimental and numerical FRF.

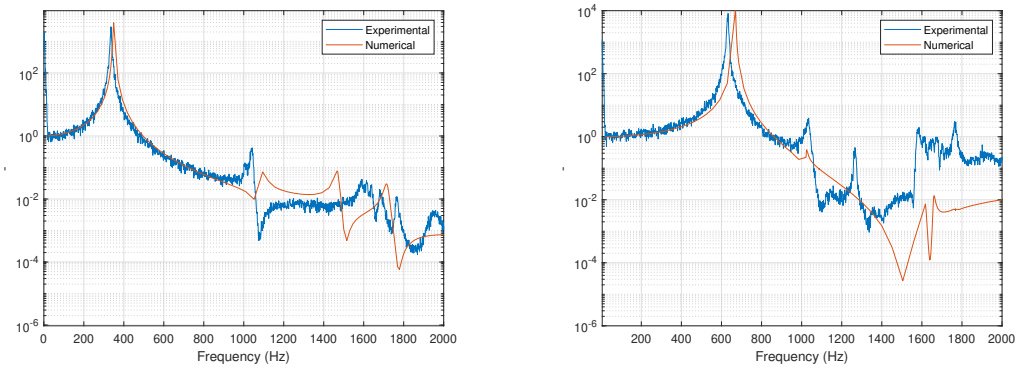

(A) Horizontal test: damping of 0.8%. (B) Vertical test: damping of 0.4%.

FIGURE 5.20: Numerical and experimental FRF with adapted damping.

Now that the damping values are correlated, the material properties are changed to switch the peak values to lower frequencies. The first interesting test consists in lowering the value of the Young modulus to 25GPa. In chapter 3, the traction test analysis showed that the combination of a Young modulus of 25GPa and a shear modulus of 4.5GPa correlated well with the experimental tests. Figure 5.21 presents the correlated results.

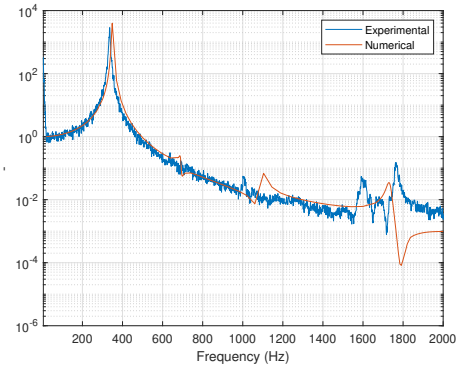

(A) Horizontal test: damping of 0.8%.

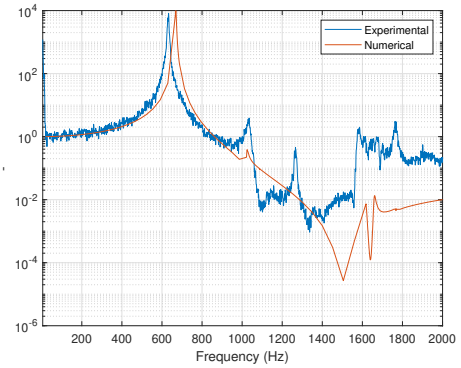

(B) Vertical test: damping of 0.4%.

FIGURE 5.21: Numerical and experimental FRF with E_{11} and E_{22} = 25GPa.

The RMS value estimated by the numerical analysis is 58.48gRMS and 60.00gRMS by experimental analysis for the vertical excitation at -12db. For the horizontal excitation at -9db, the numerical estimation is 47.19gRMS and 32.78gRMS during the experimental tests.

The first peaks in the vertical test have a difference in frequency around 30Hz. Further modifications on the GFRP properties such as varying the shear modulus and the Poisson coefficient were tested to correlate this mode but their influence is equivalent on each mode. All the modes shift to lower or higher values. The correlation on the second mode at 630Hz cannot be upgraded without loosing the correlation on the first mode. The second mode value is always overestimated.
Varying the stiffness values of the CBUSH elements does not improve the correlation.

As this mode is driven by the aluminium plate, an efficient way to adapt this mode only is to change the plate properties. However, they are considered as known and changing these values would decrease the accuracy of the material. The different boundary conditions also doesn't improve the correlation of this mode .

The final comparison in frequencies values found numerically and experimentally are shown on Table 5.5.
Only the lowest frequencies are shown as it is not possible to retrieve the exact values at frequencies higher than 1100Hz graphically. The modes are too numerous and close to be correctly evaluated. However, the Figure 5.21 shows that both the numerical and experimental models have many eigenfrequencies starting from 1600Hz to 1800Hz.

It can also be noted that through the correlation process, the mode shape did not changed.

# Mode	f_{Exp} [Hz]	$f_{Num}[Hz]$
1	337	338
3	635	666
4	692	684
5	1038	1031

TABLE 5.5: Numerical and experimental frequencies.

5.5 Conclusion

The simplified version of the aperture cylinder has a first frequency value of 337Hz. This value is close to the first frequency at 350Hz of the complex model made by GDTech presented in Figure 1.3. The model presented in this thesis is thus an acceptable simplification of the real structure.

Numerically, the fit between the eigenfrequencies is mainly based on the material properties' influence on the results. The correlation showed that the Young modulus had to fit the 25GPa found in chapter 3. However, the second frequency keeps a difference of around 30Hz with the vibration test results.
This difference can be caused by modelling uncertainties or errors or by the presence of non-linearities in the model.

The correlation can be continued by performing free-free vibration testing by hammer-hitting. This test would give the structure's shape of the different modes. A comparison between the numerical modes and the real ones would then be possible.

Chapter 6

Design improvement

6.1 Introduction

The previous chapters analysed the current design both numerically and experimentally. The different results are used to spot the weaknesses of the design. Along this chapter, alternatives to counter or reduce these weaknesses are discussed.

Material alternatives, the laminate composition and other designs are the three discussions made to explore the improvements possibilities.

6.2 Vulnerabilities and propositions

In this section, the results, comments and observations made on previous chapter are gathered to collect all the sources of vulnerabilities of the current geometries. The first discussion concerns the stacking sequences drawbacks and advantages. Then the current design observations made in chapter 4 are discussed.

6.2.1 Stacking sequence

For now, the composite used to build the structure is made out of plies stacked in the same direction. However such sequences have major drawbacks which were highlighted in this thesis. First, the behaviour is highly anisotropic. The properties of the material greatly vary depending on the orientation observed and the structure becomes sensitive in directions other that the fibres ones.

Even though such a sequence proved to sustain the loads applied during the tests, the material is still more prone to delamination. The energy dissipation area is also decreased when using an orthotropic fabric laminate compared to its quasi-isotropic counterpart and the extensional stiffness depends on the direction. The current structure is predicted to be subjected to all directions of loads and thus, stiffness along the 45° axis is also expected. The quasi-isotropic laminate thus offers more suitable performances. The numerical model build for the vibration tests used with a quasi-isotropic laminate showed that to keep a first frequency value of 337Hz, the plies of the laminate should have a Young Modulus of 27GPa in the orthotropy axes. The correlation between the experimental and numerical vibration test can be found in Appendix A.

The flexural strength of the laminate could also be improved by the use of carbon fabric plies at the extremities of the sequence. This conclusion can be found in the Nagaraja et al. [21].

6.2.2 Fillet size

The fillet size can be increased to lower the stress values. As depicted in the chapter 4, the stress concentrates around this fillet when the strut is subjected to both in-plane and out-of-plane loads. The increase of the fillet radius effects is shown in Figure 6.2. Even though the highest value of stress does not vary linearly this the fillet radius, the stress values in the whole section of the strut appear to decrease. The main effect visible is also the efforts more equally distributed between the two bolts when the fillet radius is increased. This increase in radius also increases the amount of matter which thus increases the conduction between the two stages. A quick computation can check if the design still sustains the requirement. Assuming the conduction is only made through the constant section of the strut, the 9mm fillet leads to a length of constant section of 68.9mm and the section surface is of 5x5mm. The maximal conduction between the two stages being 0.0025 W/K and the conductivity of the GFRP of 0.3, the number of struts allowed to link the two stages is:

$$N_{strut,max} = \frac{L.G_L}{S.K} = \frac{68.9x0.0025}{5x5x0.3} = 19$$

And thus, the thermal requirement would be still validated with the fillet of 9mm radius since the actual number of strut is 12.

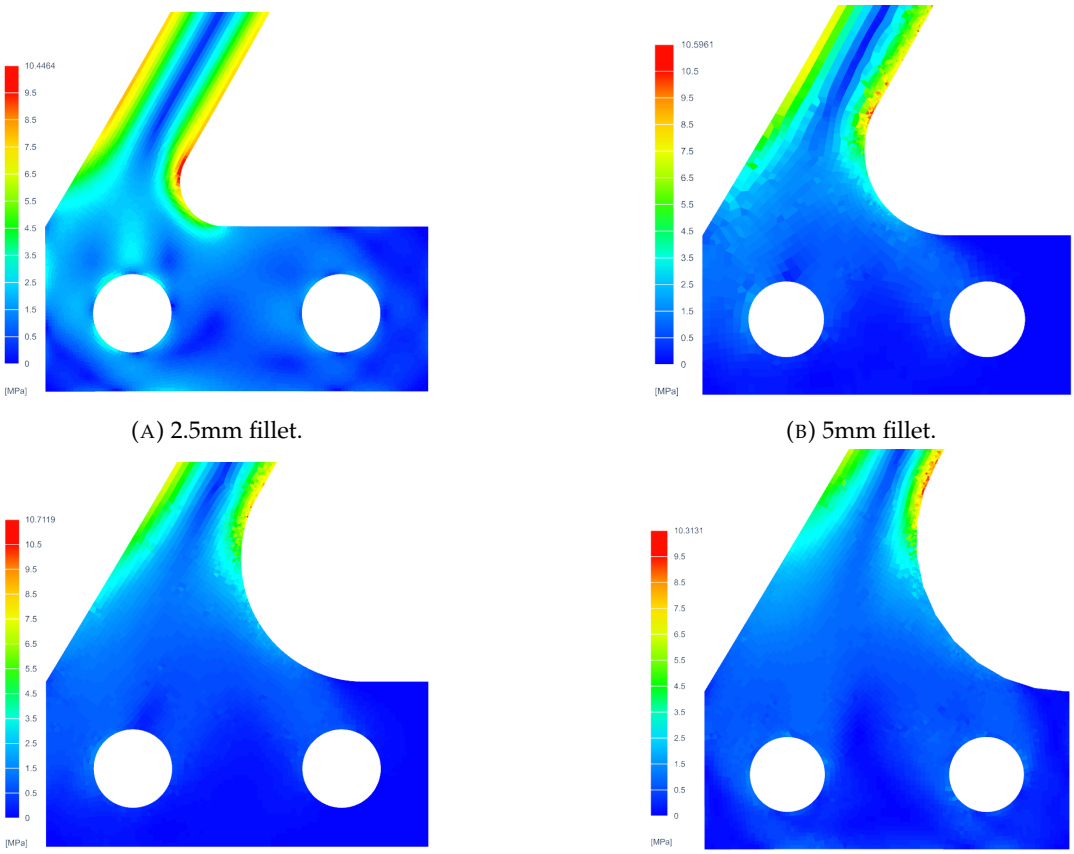

(A) 2.5mm fillet.

(B) 5mm fillet.

(C) 7mm fillet.

(D) 9mm fillet.

FIGURE 6.2: Fillet size augmentation effect on stress distribution and amplitudes.

Chapter 7

Topology optimisation

Contents

7.1 Introduction

As explained in chapter 1, the aperture cylinder's purpose is to mechanically support and connects the 100K flange with the 300K flange. It also must not amplify the other sub-systems' own resonance frequencies and shall reduce the heat transmission between the two flanges to 0.5W maximum.

The current shape of the struts met all the requirements of the mission however, it is not designed as an optimal solution for the current problem. This chapter's purpose is to discuss an optimal solution based on both thermo-mechanical and modal requirements of the aperture cylinder. A way to find an optimal shape for the aperture cylinder is the numerical method of topology optimisation.

The maximisation of conduction inside a structure is commonly analysed with optimisation tools. In the present case, one of the design objectives is to minimise the conduction. This type of optimisation is much less frequent. In parallel, the other objective of the structure design is to maximise its stiffness.

This chapter starts with a topology optimisation's general principles presentation along with the software *OOFELIE*.
A discussion about the optimisation of the aperture cylinder shape is then presented through these pages using the software *OOFELIE* topology optimisation tool. The different available functions and constraints are first presented. Then as the requirements are both based on mechanical, modal and thermal criteria, a discussion is made on the relevant way to pose the problem.
Finally, the results obtained from the different suggested cases are discussed. The results analysis covers the optimisation problems functions and constraints but also the impact of the geometry selected on the results.

On a second basis another optimisation tool, NX-TOPOL, is used for modal analysis and optimisation. The optimisation problem is also discussed and the results are compared and analysed based on the constraints and objective function set.

7.2 Topology optimisation

This section briefly presents the mathematical model and optimisation methods used in topology optimisation. This reminder aims at easing the understanding of the solver's behaviour and thus the results obtained later in this thesis.

Topology optimisation is commonly used in mechanical engineering to minimise the amount of material used while guaranteeing sufficient mechanical strength. While the meaning of "sufficient" can vary from one mission to another, an ESA-commissioned structure requires a safety factor of 1.25 with the loads leading to failure of the structure.

The mathematical methods, the *OOFELIE* software, the various optimisation functions, and the constraints that need to be overcome are all introduced in this part.

7.2.1 Optimisation principles

The main objective of topology optimisation is to present a spatial distribution of the material inside a given domain based on an objective function. This distribution is forced to validate previously established constraints. Most of the time, the objective function is unique but the constraints can be multiple for a single optimisation. At the end of an optimisation process, each element defining the domain is either filled with material or not.

The optimisation problem can be written as:

$$\text{Minimize} \quad f_{(x)} \tag{7.1}$$

$$\text{Subject to} \quad g_{j(x)} - g_j^U \leq 0, \qquad j = 1, ..., M \tag{7.2}$$

$$x_i^L \leq x_i \leq x_i^U, \qquad i = 1, ..., N \tag{7.3}$$

Material law

The convergence toward a solution with or without material elements is called a "black-and-white" solution. Indeed, the optimisation process does not immediately or always present solutions with a clear vision of which element should be kept or not. To converge to a black-and-white solution, a material law is defined. *OOFELIE* proposes multiple material laws: SIMP, RAMP, hyperbolic sine and Alpin-Tsai. The law used in this report is the SIMP law (Simply Isotropic Material with Penalisation). The solution is based on an interpolation method on the material Young modulus. This interpolation is a power law presented in Equation 7.4:

$$E_{(i)} = E_0 + \rho_{(i)}^p (E_1 - E_0) \tag{7.4}$$

Each element i thus have a modulus comprised between the values E_0 and E_1. The maximal value is simply the value of the material Young modulus. E_0 is a threshold value set to avoid ill-conditioned problems with values too close to 0 in the stiffness matrix. The penalisation parameter is usually comprised between the range [1,3]. Finally, the term ρ defines a density function whose value is comprised of between 0 and 1. A null density $\rho_{(i)}$ refers to the void and 1 to a solid element. As explained in Siva Rama Krishna, Mahesh, and N.Sateesh [24], an intermediate value can be physically interpreted as a mesostructure with holes inside.

Currently, *OOFELIE* does not support composite to define the material of the structure to be optimised. The assumption of an isotropic material is thus used to proceed to the optimisation. As stated in the previous chapters, the current laminate is made of a simple stack of plies in the same orientation. However, a quasi-isotropic laminate would be more suitable to have no preferential direction and avoid the 45° weakness of the current laminate. The laminate properties can be retrieved using the ply properties found during the correlation: $E_{ply,11} = E_{ply,22} = 25GPa$ and $G_{ply,12} = 4.5GPa$. By replacing these values in the Equation 2.17 to Equation 2.3.2, the quasi-isotropic laminate properties are a Young modulus of 20.4GPa and a Poisson coefficient of 0.28.

Optimizer

The optimizer finds the set of design variables that successfully minimise the objective function and validates the imposed constraints. It can be noted that when the objective function is maximised, the optimiser simply adds a minus to the objective function and then minimise it. *OOFELIE* optimizers are all gradient-based and thus, the sensitivities of the functions $\frac{\delta F}{\delta x}$ and $\frac{\delta C}{\delta x}$ are required to find a solution. These sensitivities are computed using the adjoint method described in Vaassen [25]. The optimizer is usually based on the MMA. The method of moving asymptotes (MMA) is presented in Hu et al. [18].

Filters

The optimisation can lead to non-physical solutions with, for example, checkerboard patterns. In these configurations, some elements with material are surrounded by empty elements. It can be instinctively understood that such a configuration is not manufacturable nor of physical interest. Filters are added to the optimisation process to avoid these instabilities. The software contains a filter either on the sensibilities or on the density and the filter radius is set to 1.5 and alters each element criteria by a weighted average with the neighbour's elements comprises in the radius distance. By doing so, a full element surrounded by empty elements has its density drastically reduced and the checkerboard effect is avoided. If necessary, the radius can be changed but it cannot be lower than the minimal element size.

Convergence limit

The optimisation being an iterative process, a limit is set to stop the computation before reaching the critical number of iterations. In this thesis, the maximal iterations are fixed to 100. This convergence criterion is set to 5% on the discreteness rate.

7.2.2 Geometry presentation

Now that all the parameters independent of the current problem are defined, the geometry is discussed. This geometry only defines two regions: The first one is the active domain. This region is defined as the space allocated for the aperture cylinder. The inner diameter of the cylinder is thus set to 230mm and the thickness is 5mm. The second region is the passive region. It represents either the filter support which cannot be removed or as it is done for the simplified numerical model presented in the previous chapters, the 100K stage simplified by a mass of 1.37kg.

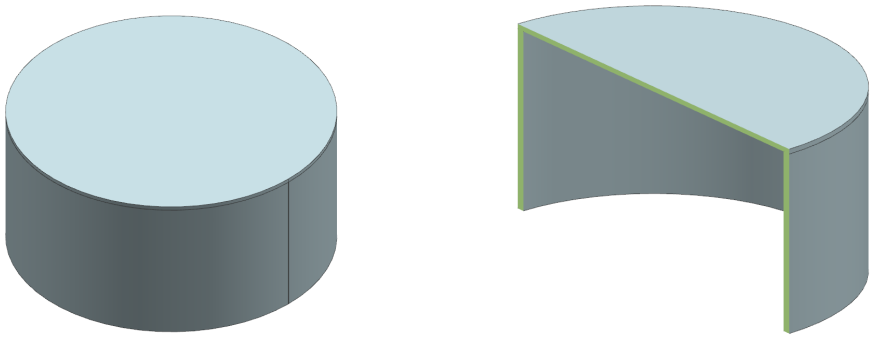

(A) Outside view. (B) Clipped view

FIGURE 7.1: Geometry of the optimisation problem.

7.2.3 Mesh

The elements used to mesh the geometry are HEXA20 solid elements of 5mm size. The number of elements along the cylinder and the 100K stage is set to be equal. The mesh is shown in the Figure 7.2.

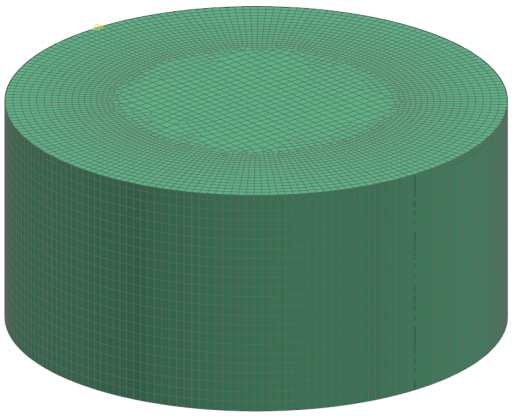

FIGURE 7.2: Geometry of the optimisation problem.

While the cylinder mesh presents a perfect symmetry, it is not the case for the cylinder at the top. This asymmetry might induce an ill-posed problem and result in non-symmetrical results even though the problem is symmetric. This hypothesis is confirmed in section 7.3 and a second geometry is thus tested by replacing the upper stage with another cylinder. This new geometry allows a fully symmetric geometry but is more dissimilar from the simplified structure presented in chapter 5 than the first one proposed. However, with the centre of the geometry cleared from any material blocking the view, it gets closer to what the real geometry could look like. Indeed, the objective of the aperture cylinder is to also support the filters and let the light pass at its centre. The only drawback is the loss of the real mass of the upper stage. A concentrated mass is added at the surface of the new 100K stage to recover a closer mass to the 1.37kg support by the aperture cylinder during the mission.

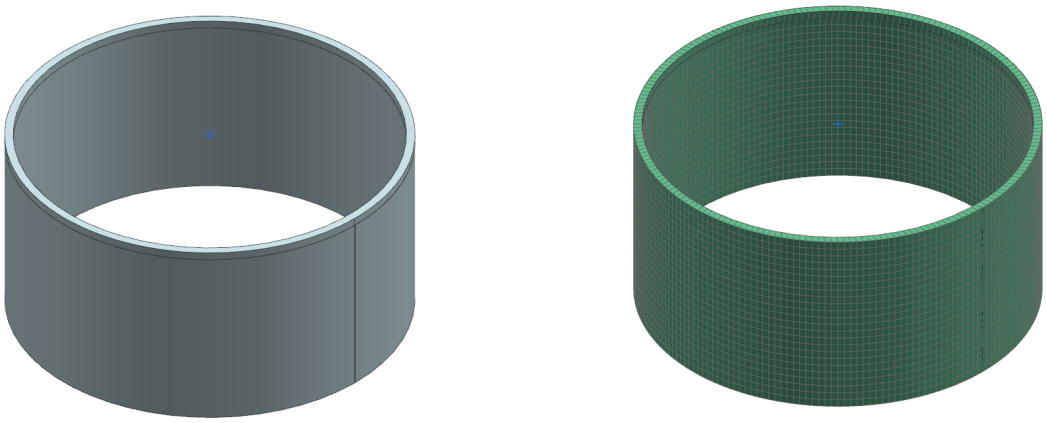

(A) Second geometry proposed. (B) Second geometry mesh.

FIGURE 7.3: Geometry and mesh for the alternative proposed.

Boundary conditions

For each optimisation problem discussed in the report, the boundary conditions remain the same: the bottom of the cylinder is fixed in translation and its temperature is fixed to 300K. It is also set as a passive region. The upper floor is a passive region and is subjected to a heat source.

7.2.4 Optimisation propositions

With the geometry now defined, a discussion on the interesting optimisation problems can start. The first step could be to analyse the solutions obtained for basic mechanical optimisation with a constraint on the volume. This first combination will determine if the geometry and meshing are sufficient to obtain an acceptable optimisation.

During the mechanical optimisation, multiple volume constraints and load cases are tested and the mechanical compliance values are tracked to be used as a reference value when another problem sets the mechanical compliance as a constraint.
It can be noted that the final geometry of the aperture cylinder cannot be based on the final solution given by this problem set as the loads applied are arbitrary and only their directions and locations are influencing the final result.
Mechanical compliance can be written as:

$$C = \frac{1}{2} u^T f_{int} u \tag{7.5}$$

where f_{int} is the vectors of the internal forces and u displacements at the nodes.

The next case presented is based on the maximisation of thermal compliance. The different constraints coupled with the objective function are a mechanical compliance, which value is based on the results obtained in the first cases studied.
The thermal compliance can be written as:

$$C_{th} = \frac{1}{2} \mathbf{T}^T f_{int} T \tag{7.6}$$

where **T** is the vector of temperature at the node.

7.3 Mechanical optimisation

The first optimisation computed is based on the minimisation of mechanical compliance. The different cases studied are presented hereafter. This section aims at spotting the potential limit of the current geometry and mesh but also to evaluate the optimised mechanical compliance value.

7.3.1 Load cases

Two cases are presented based on the mode found numerically in chapter 5. The first case is a simple normal pressure of 1MPa applied on the upper surface of the geometry and the second case presents the same pressure but tangent to the surface. In both cases, a constraint of a 0.3 volume fraction is imposed.

Case 1: normal pressure

With the first geometry presented, the black-and-white solution is obtained but the mesh asymmetry affects the solution symmetry. It can be seen on Figure 7.4a that two beams have a V-shape while the other beams are straight. There is also no symmetry with three bars on the left and two on the right. The solution obtained does not appear as a correct optimisation as some directions are more supported than others even though the loads should not induce any asymmetry in the problem.

The second geometry shows a more predictable result in Figure 7.4b with 9 V-shaped beams in cyclic symmetry. This observation justifies the hypothesis made in subsection 7.2.3 and the adaptation of the geometry to ensure a symmetrical mesh and thus, a symmetrical result.

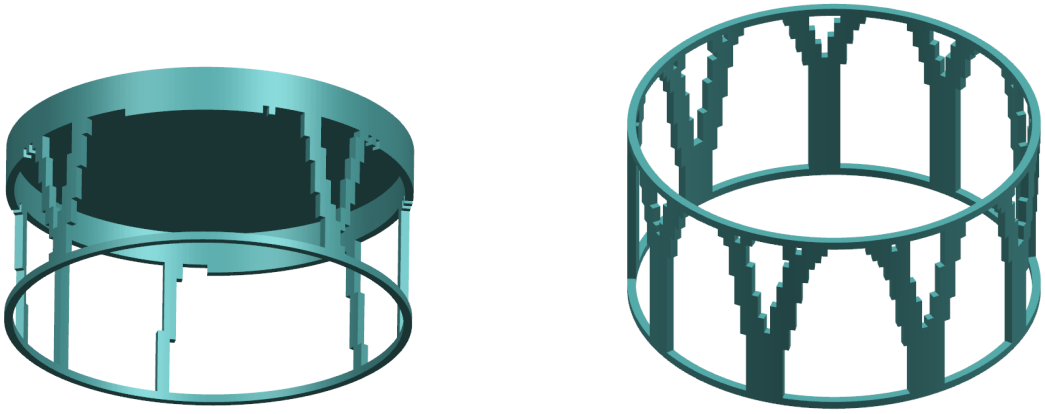

(A) First geometry. (B) Second geometry.

FIGURE 7.4: Mechanical optimisation with a volume constraint of 0.3 for normal pressure on the 100K stage.

	Geometry 1	Geometry 2
C	147.31J	69.95J

TABLE 7.1: Mechanical compliance value with a normal load.

The model is now changed by removing the passive region to see the differences between a case with and without this region. The process is done for both the first and the second geometry. The result on the first geometry is displayed in Figure 7.5. The symmetry of the problem is improved. The height bars are slightly tilted and the structure reached a compliance value of 1.46 10^8J. The convergence did not occur before the 100^{th} iteration threshold but a tendency to tilt the bar to the horizontal is barely noticeable between, for example, the iterations 70 and 100.

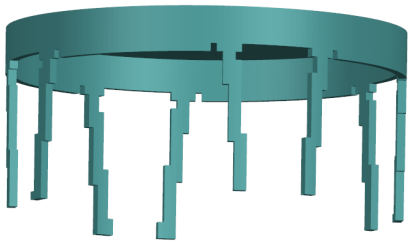

FIGURE 7.5: First geometry mechanical optimisation with a volume constraint of 0.3 for normal pressure on the 100K stage and without the bottom passive region.

Case 2: tangent pressure

In this load case, a load of 1MPa is applied tangentially to the surface. The two results obtained have different approaches with thick beams for the first geometry and thinner beam with a tilt of ±45°. The mechanical compliance of the first geometry is 1.36715 10^9J and for the second geometry, its value is 0.418J.

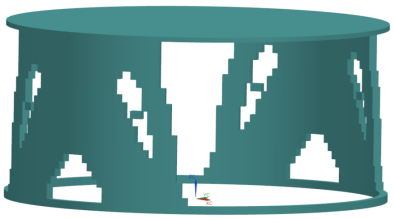

(A) First geometry.

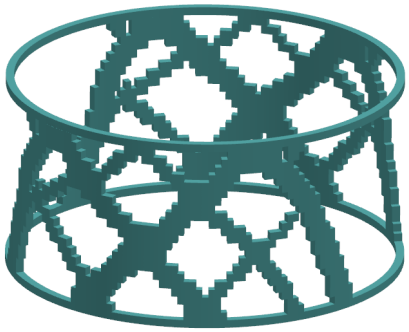

(B) Second geometry.

FIGURE 7.6: Mechanical optimisation with a volume constraint of 0.3 for tangent pressure on 100K stage.

	Geometry 1	Geometry 2
C	1.36715 10^9J	0.418J

TABLE 7.2: Mechanical compliance value with the tangent load.

7.3.2 Limitations

The topology optimisation results with a mechanical compliance function are highly dependent on the geometry of the mesh. As the first geometry is still more representative of the simplified model, the two geometries are kept to be studied for further investigations under mechanical and thermal compliance.

By investigating other optimisation constraints and function coupling, the first geometry showed issues when resolving a modal analysis. However, optimisation on the first frequency is one of the promising leads that have an actual meaning to be optimised. Indeed, as explained before, the loads applied before are arbitrary and the final shape can simply be used to evaluate the model validity and limitation and cannot lead to a final optimisation.

The first geometry is thus discarded for any modal analysis but kept for other optimisation problems.

7.4 Thermo-mechanical optimisation

7.4.1 Mechanical constraint

As the first geometry is unable to proceed to modal analysis, thermal compliance maximisation is tested with a mechanical constraint set from the results obtained in the previous section. For each case, the reference mechanical compliance is reminded and two different mechanical compliance values are tested to evaluate the influence of these parameters.

Case 1: normal pressure

The Table 7.3 recalls the values obtained from the minimisation of mechanical compliance in Table 7.1 under normal load and proposes two values to be tested during the thermo-mechanical coupling optimisation.
As the lower the value of the mechanical compliance is, the higher the stiffness of the structure, the values are selected by overestimating the mechanical compliance value. This should provide certain flexibility to adapt the structure to thermal compliance maximisation. In other terms, these new values allow a trade-off by decreasing a bit the stiffness obtained on the final structure. It can be noted that the constraint is a maximal value of mechanical compliance and thus it allows the optimisation to find a structure with lower compliance than what is set as a threshold.

	Geometry 1	Geometry 2
$C_{reference}$	147.31J	69.95J
$C_{(trial,1)}$	200.00J	100.00J
$C_{(trial,2)}$	500.00J	200.00J

TABLE 7.3: Tested mechanical compliance constraint value based on the mechanical compliance obtained from the strictly mechanical optimisation with a normal load.

The two first optimisations are done on the first geometry presented and the result after 100 iterations is presented in the Figure 7.7.

The last iteration gives the following results:

Iteration 100/100	Iteration 100/100
$f_{objective}$: $C_{th} = 1.08\ 10^{13}$J	$f_{objective}$ 1: C_{th} =4.20 10^{13}J
constraint: C = 200 $<$ 200J	constraint: C = 500 $<$ 500J

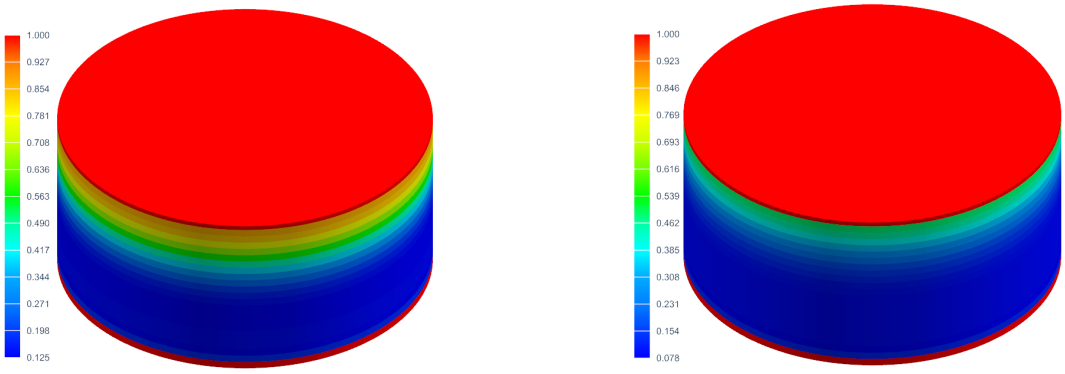

(A) $C \leq 200$J. (B) $C \leq 500$J.

FIGURE 7.7: Thermo-mechanical optimisation on density for normal pressure on the 100K stage on the first geometry.

Both results presented on the Figure 7.7 present a complete separation between the upper and lower passive domains. However, the solver assumes that the mechanical compliance inequality constraint is validated.

A similar process is now applied to the second geometry presented. Once again, the process does not end before the iteration threshold and the last iteration gives:

Iteration 100/100	Iteration 100/100
$f_{objective}$: $C_{th} = 1.8\ 10^{19}$J	$f_{objective}$ 1: C_{th} = 1.8 10^{19}J
constraint: C = $-$ 2.82 10^{7} $<$ 100J	constraint: C = $-$ 3.43 10^{7} $<$ 200J

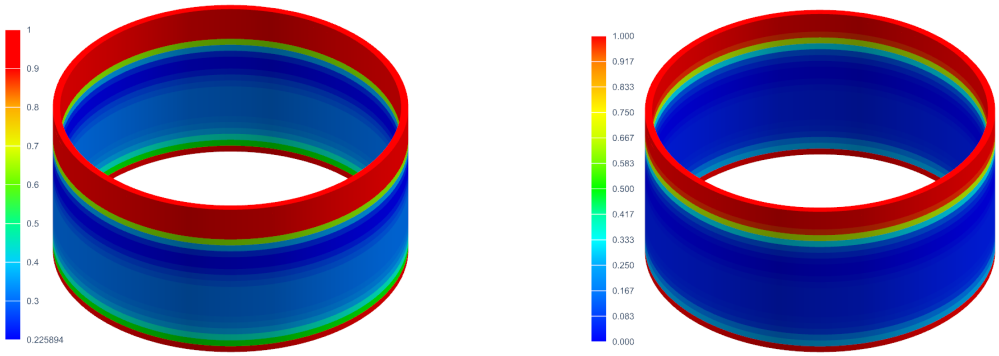

(A) $C \leq 100$J. (B) $C \leq 200$J.

FIGURE 7.8: Thermo-mechanical optimisation on density for normal pressure on the 100K stage on the second geometry.

The two passive regions are still separated. This time, however, the mechanical compliance is not validated. The value computed is not physically acceptable which already indicates the issue encountered during the optimisation.

Case 2: Tangent pressure

Since the values of the mechanical coupling were different between the two geometries, it can be interesting to see if the loading type also has an impact on the solutions. The same reflexion as presented in the normal load case is used under tangent pressure. The Table 7.2 mechanical compliance values are recalled for both geometries. These values are used to propose two mechanical compliance values as the problem constraint for both geometries. Table 7.4 presents the mechanical compliance of reference and the proposed constraints.

	Geometry 1	Geometry 2
$C_{reference}$	1.37 10^9J	0.42J
$C_{(trial,1)}$	5.00 10^9J	1.00J
$C_{(trial,2)}$	10.00 10^9J	2.00J

TABLE 7.4: Trial mechanical compliance constraint value with a normal load.

The first geometry results are presented in the Figure 7.9.

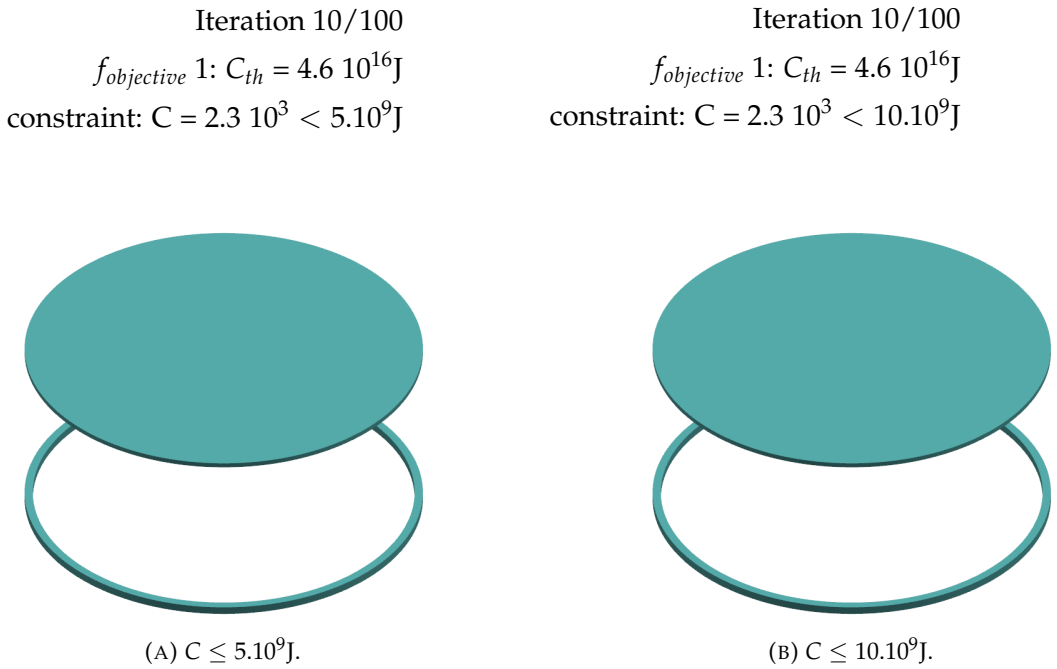

(A) $C \leq 5.10^9$J. (B) $C \leq 10.10^9$J.

FIGURE 7.9: Thermo-mechanical optimisation on density for tangent pressure on the 100K stage on the first geometry.

This time, the convergence occurs before the 100 iterations. The results are black and white. The Figure 7.9 shows the final structure kept. The structure is still separated but the mechanical compliance gives a positive low value. The two solutions are the same as the optimal compliance value found is lower than the two thresholds imposed.

Finally, the second geometry results are presented in the Figure 7.10.

Iteration 100/100
$f_{objective}$ 1: C_{th} = 1.8 10^{19}J
constraint: C = 1.4 10^{4} < 1J

Iteration 100/100
$f_{objective}$ 1: C_{th} = 4.7 10^{15}J
constraint: C = 14.3 < 2J

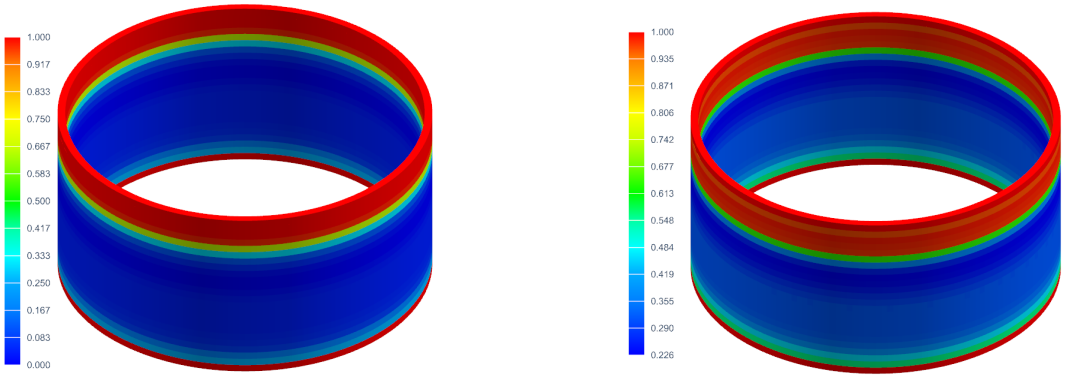

(A) C ≤ 1J. (B) C ≤ 2J.

FIGURE 7.10: Thermo-mechanical optimisation on density for tangent pressure on the 100K stage on the second geometry.

The solution does not converge anymore for either constraint or validates the constraint. Even though the final mechanical compliance value is positive, during the iteration process, the value kept switching between positive and negative values.

7.4.2 Limitations

Through the study of the optimisation problem, thermal optimisation appeared to remove any connection between the heat source and the fixed temperature. As it is indeed the most effective way to maximise thermal compliance and thus reduces the conductivity between the two stages, it ignores the mechanical requirement.

The issue has been addressed to the developers but is not resolved at the time of the thesis. Another way to reduce the conductivity has to be investigated without any upgrade of the coupling between the two constraints.

7.5 Modal and thermal optimisation

Now that the coupling between mechanical and thermal coupling has been analysed, another coupling is tested: thermal compliance and the first resonance frequency. In this section, the thermal compliance is still maximised but the inequality constraint is changed to have a minimal first frequency value.

It can be noted that setting the upper stage as a passive domain is necessary to obtain a concluding result. Otherwise, if the frequency is maximised, the height of the cylinder is simply reduced.

The first geometry cannot provide a satisfying result for a modal analysis as it gives frequencies of 0Hz or with an infinite value. A static case has been made to spot any problem in the mesh or the connections but no error has been detected. Other definitions of the same geometry have also been tested to allow modal analysis without success.

With a modal analysis on the second geometry proposed, the first frequency is null and four other positive values frequencies. The shape of the first mode is not a rigid body mode even though the frequency is equal to 0. During an optimisation on the frequency, the first frequency is the null frequency found during the strictly modal analysis and cannot modify its value. The results obtained by the optimisation only keep the passive regions. Any other element has a null density. Thus, the structure is once again split into two pieces.

A new geometry is tested with only one cylinder. This avoids the use of gluing or fitting the nodes of different meshes.

The first optimisation tested with a modal analysis is a maximisation of the thermal coupling and maximising the first frequency to a value higher than 150Hz as it is the primary requirement on the structure.

7.5.1 New geometry

To avoid any error during the modal analysis, a new model, even more simplified is created to avoid the mechanical gluing or the need to fuse two nodes as this tool doesn't solve the frequency issue either. The Figure 7.11 present the new geometry.

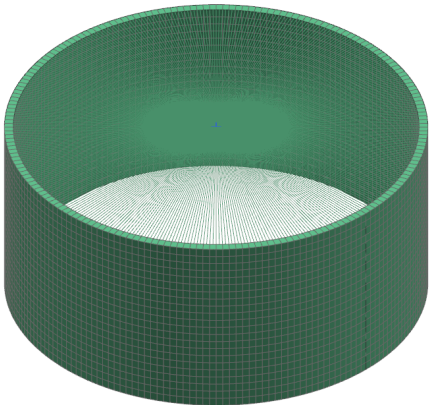

FIGURE 7.11: Third geometry proposed.

The new model is a simple cylinder with the same geometry as the main cylinders presented in the two previous models. The 100K stage is removed and replaced by rigid links linking the inner diameter nodes to a central node. Finally, a mass of 1.37kg is imposed at the centre node to simulate the weight imposed by the 100K stage.
The constraints are not different from the ones imposed previously with the bottom fixed in translation and the upper surface being a heat source. The central node cannot be the source of the heat source as it is a strictly mechanical element thus, it cannot support a thermal load.

7.5.2 Optimisation cases

With the new geometry now defined, the different optimisations to be tested are discussed. All the optimisations have the maximisation of thermal compliance as it was done in the previous section. The inequality constraint imposes a minimal value of the first frequency: 150, 350 or 500Hz. After these optimisations tests, additional constraints are discussed such as the addition of a volume constraint.
The optimisation problems can be written as:

$$\begin{aligned} &\text{Minimize} && C_{th} && \\ &\text{Subject to} && f_{r,1} \geq 150\text{Hz} && \text{(Case 1)} \\ &&& \quad\ 350\text{Hz} && \text{(Case 2)} \\ &&& \quad\ 500\text{Hz} && \text{(Case 3)} \end{aligned}$$

Case 1: $f_{r,1} > 150$ **Hz**

The first case optimised structure is displayed in Figure 7.12. The solution converged before the 100 iterations and is black and white.

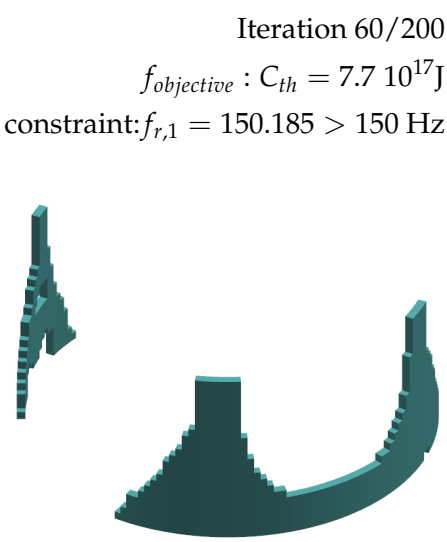

FIGURE 7.12: Structure optimised for a minimum of 150Hz and maximal thermal compliance.

The constraint is validated and the thermal compliance value is in the positive domain. On the Figure 7.12, the structure is divided into three beams. Two of them are linked by a horizontal beam.

Case 2: $f_{r,1}$ > 350Hz

The second test only increases the minimal frequency to 350Hz. The resulting structure is displayed in Figure 7.13. Once again, the solution converged and is black and white.

Iteration 20/200
$f_{objective}$: C_{th} = 4.2 10^{17}J
constraint: $f_{r,1} = 350 > 350$ Hz

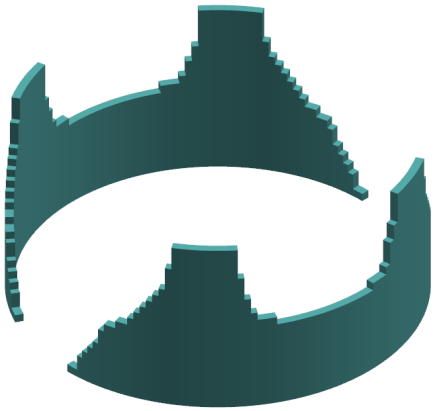

FIGURE 7.13: Structure optimised for a minimum of 350Hz and maximal thermal compliance.

The structure is still divided in two, as it is done in the first case. However, the solution is now symmetric, the number of beams increased to four and their base is thicker. The number of elements kept at the base is 10 which corresponds to a length of ~36mm. The first frequency's value is the lowest possible as it was the case for the 150Hz frequency limit in case 1.

The thermal compliance decreased by a factor of ~1.83 and is the consequence of the increase in mass between the two structures as the number of beams and the thickness of the base and beams increased.

Case 3: $f_{r,1} > 500$ Hz

The final constraint frequency is now tested. Figure 7.14 presents the results. The solution converged and is black and white.

Iteration 121/200
$f_{objective}$: C_{th} = 3.3 10^{17}J
constraint: $f_{r,1} = 500 > 500$ Hz

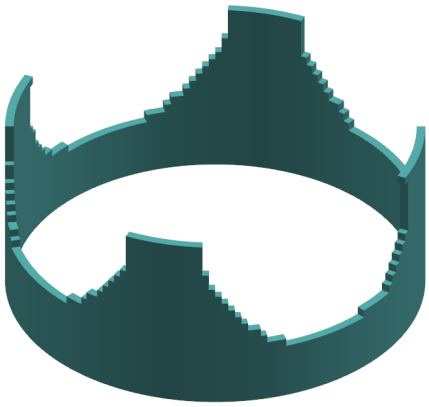

FIGURE 7.14: Structure optimised for a minimum of 500Hz and maximal thermal compliance.

The beams are still four and their base thickness increased to 12 elements which correspond to ~43mm. The main difference between this structure and the solution proposed by the optimisation in case 2 is the link between the four bars. As it was the case between cases 1 and 2, increasing the minimal frequency value decreased the thermal compliance once again with the addition of material.

Addition of constraints

The increase of minimal frequency induced an increase in the final volume of material. A constraint on the volume fraction is added to the frequency minimal value. The test is made in addition to the 150Hz but also the 500Hz constraints.

Iteration 200/200
$f_{objective}$: C_{th} = 9.0 10^{17}J
constraint 1: $f_{r,1} = 246.799 > 150$ Hz
constraint 2: V =119661 $>$ 119607

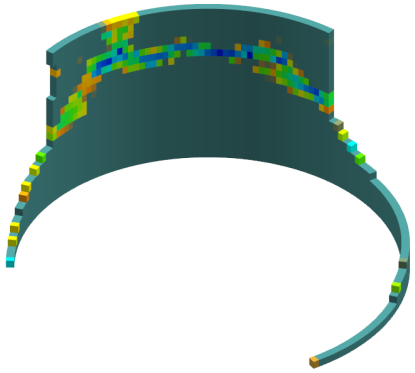

FIGURE 7.15: Structure optimised for a minimum of 500Hz and maximal thermal compliance.

The solution provided does no converges before the 200 iterations but the shape formed can already predict an unsatisfying final structure. The asymmetry of the structure cannot validate the requirement imposed by the requirements. This asymmetry is lost through the iterations meaning that the symmetry cannot be kept to fulfil all the requirements.

The optimisation obtained using 500Hz as the minimum value produces an all-empty domain after attempting to find a symmetric shape.

7.6 Modal optimisation with TOPOL

As some issues were found during modal analysis using *OOFELIE* which couldn't be resolved in the period of this thesis, another software is used to perform topology optimisation based on a modal analysis: TOPOL. The optimisation is made in two steps:

1. Frequency as the objective function and the volume constrained
   (a) V > 0.3%
   (b) V > 0.6%
2. Volume as the objective function and the frequency constrained
   (a) f > 150 Hz
   (b) f > 350 Hz

For the first step, the frequencies are maximised. For the second step, two different minimal frequencies are tested to constrain the problem: 150Hz and 350Hz. The first frequency is selected to perfectly fit the first frequency requirement and the second one to get a margin with the requirement but also to have a similar frequency as the one found when studying the current design in chapter 5. Finally, symmetry constraints are discussed.
The interpolation method selected is the SIMP method with the SPOT optimizer. A limit of 100 iterations and a convergence threshold of 0.4% are set for each optimisation.

7.6.1 Frequency maximisation

Constraint: V < 0.6%

Figure 7.16 shows the optimised results of the frequency maximisation of the design domain after 100 iterations for a target volume inferior to 0.6%. The optimisation did not converge up to the threshold set but reached a convergence rate of 93%. The results do not present any symmetry and the frequency value obtained is more than 4 times the frequency requirement of 150Hz.

As the optimisation did not reach the convergence threshold set, the frequency value is not precise. Figure 7.17 shows that the frequencies' values were not fully stabilised.

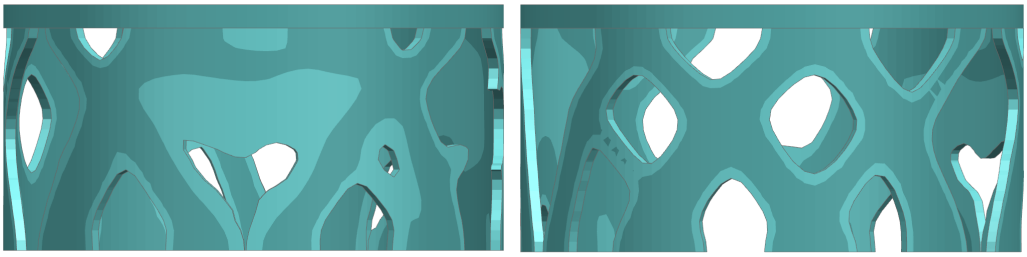

(A) Side I. (B) Side II.

FIGURE 7.16: Optimised domain under constraint V < 0.6%. $f_1 = 636$ Hz (density > 0.8 and lattice > 0.5).

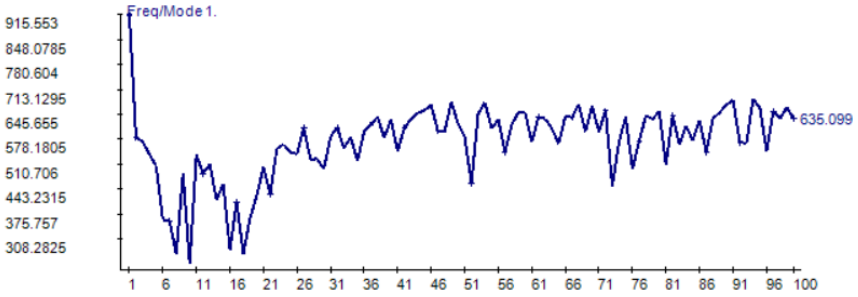

FIGURE 7.17: First frequency through the iterations for 0.6% constrain on volume.

Constraint: V < 0.3%

Figure 7.18 presents the optimised structure when the constraint on the volume is decreased down to 0.3%. The frequency found dropped around 300 Hz but does not show a cyclic symmetry. The convergence reaches a value of 96.5%. A cyclic symmetry of 120° is thus imposed based on the result proposed without symmetry and the convergence reaches 98%. Figure 7.19 presents the first frequency value during the iteration process.

(A) no symmetry applied. $f_1 = 297$. (B) Symmetry at 120°. $f_1 = 324$.

FIGURE 7.18: Optimised domain under constraint V < 0.3%. Hz (density > 0.8 and lattice > 0.5).

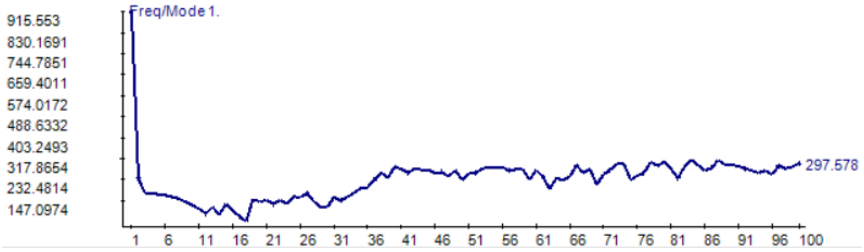

(A) Without symmetry.

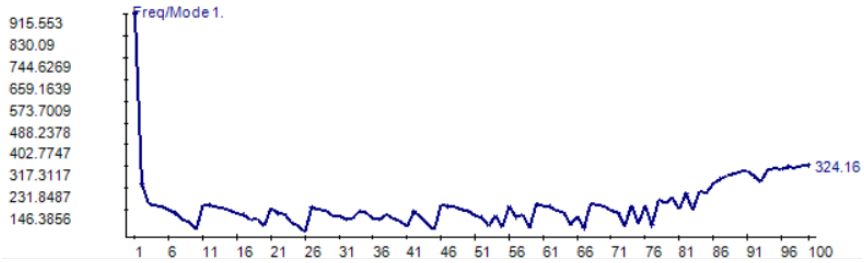

(B) With a 120° cyclic symmetry.

FIGURE 7.19: First frequency through the iterations with a 0.3% constrain on volume.

7.6.2 Volume minimisation

Constraint: $f_{r,1} > 150$ **Hz**

The convergence reaches a value of 98% and the frequency value oscillates below the 150Hz as it can be seen in Figure 7.20.

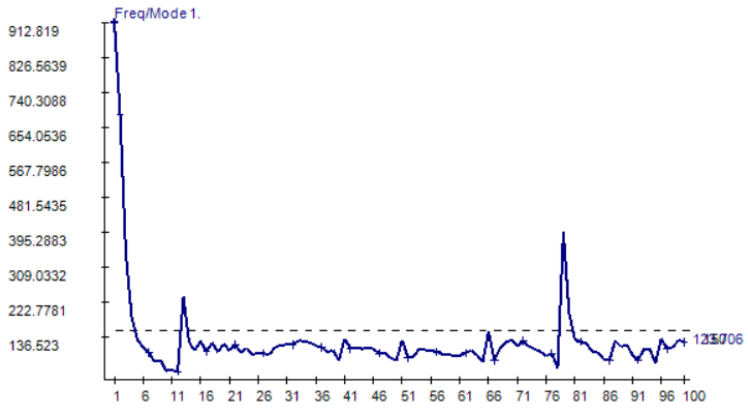

FIGURE 7.20: First frequency through the iterations with a minimal frequency of 150Hz.

Figure 7.21 shows the final volume obtained after 100 iterations. The solution shows beams in a cross shape. The frequency of the first mode below the 150Hz requirement with a final value of 125Hz. It also provides an asymmetric solution probably since the mesh is also asymmetric at the upper stage. A cyclic condition can force the symmetry and is studied in subsection 7.6.3.

FIGURE 7.21: Optimised domain for >20% density, $f_1 = 125$ Hz.

Constraint: $f_{r,1} > 350$ **Hz**

When increasing the minimal frequency to 350Hz, the behaviour of the convergence is similar that presented in Figure 7.20 with an oscillating value below 350Hz.

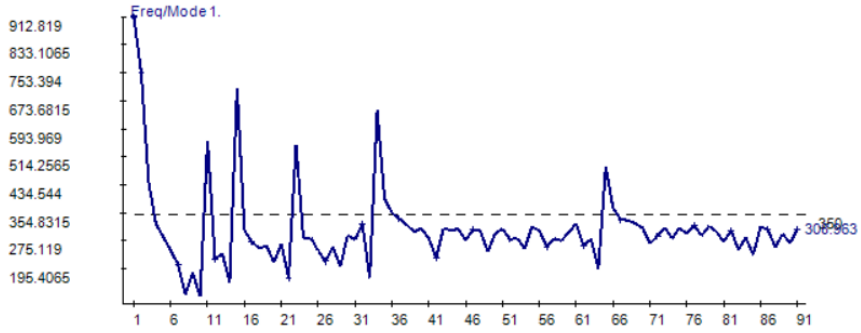

FIGURE 7.22: First frequency value for each iteration with 0.3 target volume.

The result is symmetric and the beams are placed in a V-shape. The quantity of material also increased compared to the 150Hz threshold.

FIGURE 7.23: Optimised domain for >50% density, $f_1 = 308$ Hz.

7.6.3 Symmetry constrain study for $f_{r,1} > 350$ Hz

Different symmetries are now tested. As the 150Hz constraint does not ensure actually finding a frequency value above 150Hz, the studied constraint is 350Hz. Four symmetries are forced: 3, 4, 5 and 6 cyclic repetitions and are presented in Figure 7.24. It can be noticed that the higher the cyclic symmetry imposed is, the lower the first frequency found is.

(A) Cyclic symmetry of 120°. $f_1 = 315$ Hz.

(B) Cyclic symmetry of 90°. $f_1 = 308$ Hz.

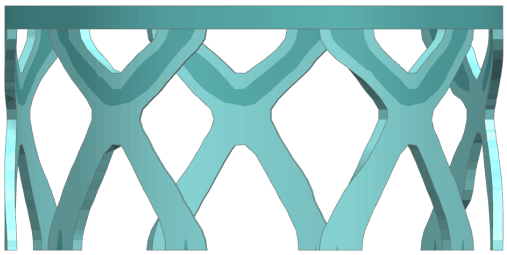

(C) Cyclic symmetry of 72°. $f_1 = 250$ Hz.

(D) Cyclic symmetry of 60°. $f_1 = 170$ Hz.

FIGURE 7.24: Volume minimisation with $f > 350$ Hz optimized structure (density > 0.8 and lattice > 0.5).

7.7 Further discussions

For now, *OOFELIE* does not support composite as a material to be optimised. However, as composites rise in many engineering applications, the fibre orientation optimal distribution also appears as an interesting work field. The matter has already been discussed notably in Bruyneel, Duysinx, and Fleury [6] and the adaptation of the *OOFELIE* solver is possible for further improvements on the composite field.

Another improvement interesting focus on the loads. For now, the solver automatically keeps the elements subjected to a mechanical load. In the different optimisation analyses, the mechanical loads had to be applied on either a passive surface or rigid elements to create a separation between the active domain and the loads. Another solution is to modify the geometry directly to consider that the elements attached to the load are automatically kept. A possibility could be to distribute the load attached to an empty element to the surrounding elements.

7.8 Conclusion

The model had to be adapted to proceed to a modal analysis. The two first geometries tested cannot perform a correct modal analysis. Various parameters were modified to find the sources of this issue notably the separation of the upper ring of the geometry 1 to perform multi-physic gluing on almost equal surfaces, but also the substitution of the *multiphysic gluing* tool by the *equal nodes* tool. Static simulations were also performed to spot nodes unattached.

After these tests, the most simple geometry is created and the upper stage is replaced by simple rigid links and a central mass equal to the mass of the stage tested

in chapter 5. The same optimisation constrains on both the mechanical and thermal compliances as it is done in section 7.3 were performed but the outcome was similar.

As a result, the combination of thermal and mechanical compliance cannot be conducted in case the maximal value of thermal compliance is searched. No issues were found when the conduction is maximised and thus the thermal compliance is minimised. Only the maximisation of the thermal compliance is an issue.

This kind of optimisation problem, even though it did not have a direct interest in the present case, is still valuable to be investigated. Common problems can be based on the loads encountered and minimising the conduction between interfaces is also very common, especially in the space industry. An interesting approach for the design of a component could be the combination of different load cases with equal importance on the structure such as a side load and a load from the Z-axis. Combined with an imposed symmetry and thermal coupling, a repeated shape might be found.

As the third geometry proposed using *OOFELIE* does not represent with accuracy the real geometry of the problem, the solver *NX-TOPOL* is used to perform modal analysis and optimisation. The results presented in Figure 7.24b had a similar geometry as the strut presented and the shapes suggested in Figure 7.24d and Figure 7.24c could be interesting to study in more details.

Further investigation could also be done by increasing the number of elements contained in the cylinder's thickness to see if the optimizer uses this thickness. During the many tests performed aside from the ones shown in this thesis, such configuration was tested but the results did not provide clear use of the thickness. The process could be tested on thicker allowed volume. However, simply tilting a composite beam would greatly increase the forces out of the laminate plane applied by the upper stage. As it is demonstrated in the test performed in chapter 4, the composite has high displacement in bending even for small forces so it might reduce the structure performance.

Chapter 8

Conclusion

This thesis focused on the in-depth analysis of a sub-system of the space telescope Athena: the aperture cylinder. Before the start of the thesis, the GFRP was selected as a suitable material to build the ApC. A GFRP laminate made for low temperature conditions was also ordered. A complex CAD model with a modal analysis had been made by *GDTech*. Two different designs were suggested. The first design of the ApC consisted of three beams supporting the 100K flange. The second design introduced a geometry aiming at minimising the thermal flux between the two stages supported by the ApC. The ApC shapes then resulted in 12 struts in a Z-shape. The modal study made by *GDTech* on the ApC with the strut design had a first frequency of around 350Hz.

This thesis had multiple goals for the design of the aperture cylinder that can be split into two parts. The first part of this thesis studied extensively the current choice for the design. The second part used topology optimisation to suggest different shapes of ApC. As the Athena mission is currently in a redesign phase, this thesis aims at giving a general approach to the ApC design.

The first step of the thesis performed a preliminary material selection and validated the use of GFRP. Then, the study focused on the thermal and mechanical properties of the GFRP samples ordered. The first estimation of the plies properties was based on the observation made on the sample, common glass-fibre laminates properties and the lamination theory. The plies properties were deduced from two UD plies stacked one above the other with a 90° orientation difference. The laminate properties have then been deduced with lamination theory based on two different hypotheses. The first one suggested a quasi-isotropic laminate and the second a sequence of plies in the same direction. A spectroscopy on a laminate sample was performed to evaluate the stacking sequence but the results couldn't give any information on the sequence.

Then traction tests were performed on samples with different fibre orientations. The traction results showed significant differences in behaviour between the different orientations. This observation validated the unidirectional stacking sequence hypothesis. A numerical analysis reproduced the traction samples' margin of safety distribution in the laminate and the traction tests failure occurred at the location of failure numerically predicted. The actual traction force to break the laminate couldn't be evaluated numerically as it required to perform a nonlinear material model. From the traction results, two properties estimated in the first part were corrected: a Young modulus of the laminate of 25GPa obtained with the curve of the stress-strain curve, and the shear modulus of 4.5GPa using a numerical simulation

and a correlation with the experimental test.

The next step of the thesis focused on both the experimental and numerical study of the single strut composing the ApC. This part presented the behaviour of the strut under bending and flexion and the stress distribution for the corresponding loads.

Finally, the CAD made by *GDTech* was simplified using the stiffness of the 100K flange to reduce this flange shape to a simple dodecagon. A numerical model is then built, extensively described and studied to reproduce the vibration tests performed on a shaker. Various aspects of the model are studied to evaluate its sensibilities and justify the choices made. The mode shapes and resonance frequencies are evaluated. The vibration tests on the shaker are described. The structure supported the 25G required and showed greater displacements when the vertical axis has been excited. The frequencies were retrieved from the test and gave a first frequency of 337Hz. The correlation with the numerical model was mainly based on the damping coefficient evaluation as the first frequency value is correlated with the material properties deduced from the traction tests. The next step to studying further the simplified structure could be the study of a free-free vibration test with hammer hitting. This test would retrieve the real mode shape of the structure and the difference between the experimental and numerical mode could be done using a MAC matrix. The efforts in the screws could also be done more extensively as the screw holes weaken the laminate as it breaks the fibres.

The conclusion made from the traction tests and the strut design led to the suggestion of design improvements. First, a discussion on the use of a quasi-isotropic laminate is made. The numerical model built for the vibration tests showed that to keep a first frequency value of 337Hz, the plies of the laminate should have a Young Modulus of 27GPa in the orthotropy axes. This solution would increase the performance of the struts in other directions than the material axis and would also decrease the risk of failure.
On a second basis, the fillet influence on the stress distribution is evaluated along with its influence on the thermal flux increase induced by the fillet radius increase. The thermal flux between the two stages validated the thermal requirement even with the fillet radius increased at the maximal value.

The second part of the thesis explored the possibility of thermo-mechanical optimisation. The first 3D multidisciplinary design software used is *OOFELIE* from *Open Engineering*. During the discussion on the different relevant optimisation problems, the maximisation of thermal compliance did not provide satisfying results as it removed completely the optimisable domain. Issues were also spotted during the modal analysis of the geometry. It was thus decided to switch with the *TOPOL* topologic optimiser tool to perform modal optimisation and multiple geometries are suggested for different cyclic symmetries proposed. One of the optimised structure resembles the 12 struts design.

Appendix A

Vibration testing results

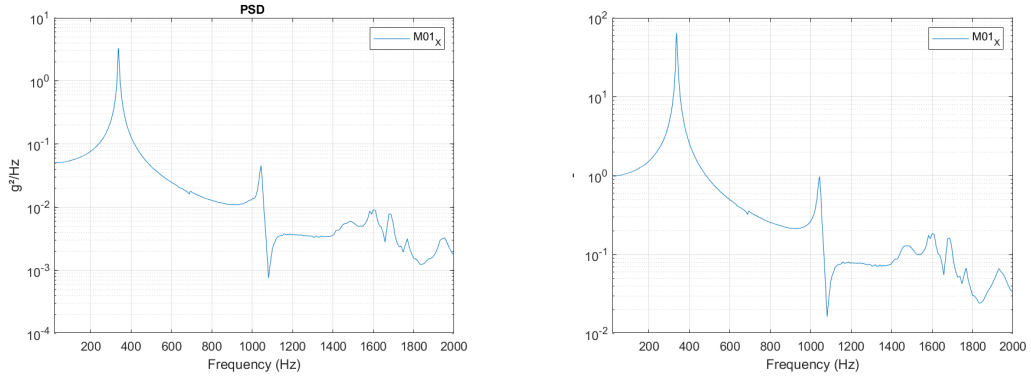

(A) PSD. (B) FRF.

FIGURE A.1: Experimental results of the horizontal sine-sweep vibration test.

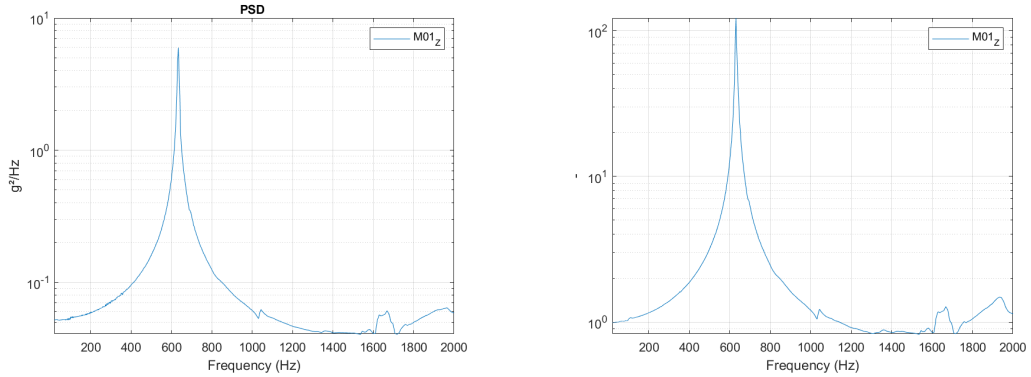

(A) PSD. (B) FRF.

FIGURE A.2: Experimental results of the vertical sine-sweep vibration test.

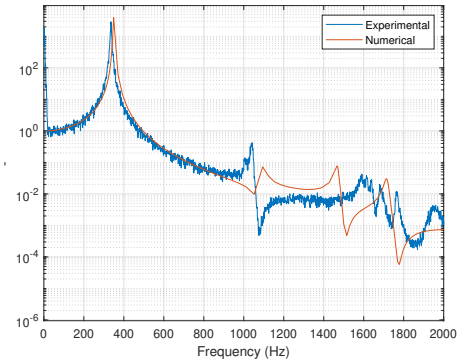

(A) Horizontal test: damping of 0.8%.

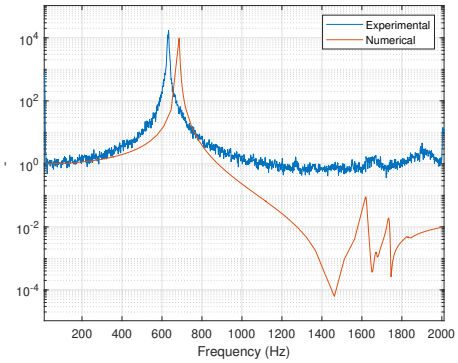

(B) Vertical test: damping of 0.4%.

FIGURE A.3: Correlated FRFs for quasi-isotropic laminate.

Bibliography

[1] *Aperture cylinder DM2 : FEM random analyses status*. GDTech, May 2022.

[2] *Athena XIFU - Aperture Cylinder Design Description*. Centre Spatial de Liège, Oct. 2022.

[3] Jean-Marie Berthelot et al. "Damping analysis of composite materials and structures". In: *Composite Structures* 85.3 (2008), pp. 189–204. ISSN: 0263-8223. DOI: https://doi.org/10.1016/j.compstruct.2007.10.024. URL: https://www.sciencedirect.com/science/article/pii/S0263822307002528.

[4] M. Bruyneel and C. Fleury. "Composite structures optimization using sequential convex programming". In: *Advances in Engineering Software* 33.7 (2002). Engineering Computational Technology Computational Structures Technology, pp. 697–711. ISSN: 0965-9978. DOI: https://doi.org/10.1016/S0965-9978(02)00053-4. URL: https://www.sciencedirect.com/science/article/pii/S0965997802000534.

[5] Michael Bruyneel. "Schémas d'approximation pour la conception optimale de structures en matériaux composites". In: 2002.

[6] Michaël Bruyneel, Pierre Duysinx, and Claude Fleury. "A family of MMA approximations for structural optimization". English. In: Harrogate, United Kingdom, July 2001.

[7] *Composite Material Handbook*. Vol. 2, POLYMER MATRIX COMPOSITES MATERIALS PROPERTIES. 2018.

[8] Isaac M. Daniel, Jyi-Jiin Luo, and Patrick M. Schubel. "Three-dimensional characterization of textile composites". In: *Composites Part B: Engineering* 39.1 (2008). Marine Composites and Sandwich Structures, pp. 13–19. ISSN: 1359-8368. DOI: https://doi.org/10.1016/j.compositesb.2007.02.002. URL: https://www.sciencedirect.com/science/article/pii/S1359836807000327.

[9] Alfred Djoumessi et al. "Optimization of the Young's modulus of woven composite material made by Raphia vinifiera fiber/epoxy". In: *International Journal for Simulation and Multidisciplinary Design Optimization* 13 (Oct. 2022). DOI: 10.1051/smdo/2022014.

[10] *DOD/NASA Advanced Composites Design Guide*. Item 0001, Sequence. Rockwell International. North American Aircraft Operations. Air Force Wright Aeronautical Laboratories, Flight Dynamics Laboratory, Structures/Dynamics Division, 1983. URL: https://books.google.be/books?id=pHqGuAEACAAJ.

[11] *ECSS-E-ST-32-10C Rev.1 - Structural factors of safety for spaceflight hardware*. European Cooperation for Space Standardization. Mar. 2009.

[12] *ECSS-E-ST-32-11C - Modal survey assessment*. European Cooperation for Space Standardization. July 2008.

[13] *ECSS-Q-ST-70-02C - Thermal vacuum outgassing test for the screening of space materials*. European Cooperation for Space Standardization. Nov. 2008.

[14] *ECSS-E-ST-10-03 — Testing*. European Cooperation for Space Standardization.

[15] *ECSS-E-ST-32 — Structural general requirements*. European Cooperation for Space Standardization.

[16] *ECSS-S-ST-00-01 - Glossary of terms*. European Cooperation for Space Standardization.

[17] C. Fleury and V. Braibant. "Structural optimization: A new dual method using mixed variables". In: *International Journal for Numerical Methods in Engineering* 23 (1986), pp. 409–428.

[18] Xueyan Hu et al. "An adaptive method of moving asymptotes for topology optimization based on the trust region". In: *Computer Methods in Applied Mechanics and Engineering* 393 (2022), p. 114202. ISSN: 0045-7825. DOI: https://doi.org/10.1016/j.cma.2021.114202. URL: https://www.sciencedirect.com/science/article/pii/S0045782521005338.

[19] Brett A. Bednarcyk Jacob Aboudi Steven M. Arnold. *Practical Micromechanics of Composite Materials*. Elsevier, July 2021.

[20] Qingxuan Meng et al. "Lightweight topology optimization of thermal structures under compliance, stress and temperature constraints". In: *Journal of Thermal Stresses* 44.9 (2021), pp. 1121–1149. DOI: 10.1080/01495739.2021.1958721. eprint: https://doi.org/10.1080/01495739.2021.1958721. URL: https://doi.org/10.1080/01495739.2021.1958721.

[21] K.C. Nagaraja et al. "Studying the effect of different carbon and glass fabric stacking sequence on mechanical properties of epoxy hybrid composite laminates". In: *Composites Communications* 21 (2020), p. 100425. ISSN: 2452-2139. DOI: https://doi.org/10.1016/j.coco.2020.100425. URL: https://www.sciencedirect.com/science/article/pii/S2452213920301534.

[22] Xueyong Qu et al. "Thermal Topology Optimization in OptiStruct Software". In: June 2016. DOI: 10.2514/6.2016-3829.

[23] Osvaldo M. Querin et al. "Chapter 3 - Discrete Method of Structural Optimization**Additional author for this chapter is Prof. Dr.-Ing. Dr.-Habil. George I. N. Rozvany." In: *Topology Design Methods for Structural Optimization*. Ed. by Osvaldo M. Querin et al. Oxford: Academic Press, 2017, pp. 27–46. ISBN: 978-0-08-100916-1. DOI: https://doi.org/10.1016/B978-0-08-100916-1.00003-9. URL: https://www.sciencedirect.com/science/article/pii/B9780081009161000039.

[24] L. Siva Rama Krishna, Natrajan Mahesh, and N.Sateesh. "Topology optimization using solid isotropic material with penalization technique for additive manufacturing". In: *Materials Today: Proceedings* 4.2, Part A (2017). 5th International Conference of Materials Processing and Characterization (ICMPC 2016), pp. 1414–1422. ISSN: 2214-7853. DOI: https://doi.org/10.1016/j.matpr.2017.01.163. URL: https://www.sciencedirect.com/science/article/pii/S2214785317301633.

[25] Jean-Marc Vaassen. *Topology optimization Theory*. Open-Engineering S.A.